Journal of Materials Chemistry A

ROYAL SOCIETY OF CHEMISTRY

REVIEW

View Article Online
View Journal | View Issue

Cite this: J. Mater. Chem. A, 2025, 13, 17242

Recent advances in Cu-based intermetallics: structures, syntheses, and electrocatalytic applications

Bo Chen, *[a] Peiyu Duan,[a] Shuo Wang,[a] Hanyun Pan,[a] Shuxian Wu,[a] Ye Hua,[a] Xingyu Tao,[a] Qinbai Yun *[bc] and Yonghua Li *[a]

Received 26th March 2025
Accepted 24th April 2025

DOI: 10.1039/d5ta02448j

rsc.li/materials-a

Recent advancements in Cu-based intermetallics have sparked significant interest in electrochemical energy conversion and related fields. This review focuses on the latest developments in Cu-based intermetallics, covering their structures, synthesis methods, and electrocatalytic applications. We first classify the structural types of Cu-based intermetallics and explore the thermodynamic and kinetic factors influencing their formation. Key synthesis techniques, such as thermal annealing and liquid-phase methods, are discussed, alongside strategies for size and morphology control. The applications of Cu-based intermetallics in electrocatalysis, including the hydrogen evolution reaction, carbon dioxide reduction reaction, oxygen reduction reaction, and nitrate reduction reaction, are then examined in detail. Lastly, we demonstrate the challenges in this area and suggest future research directions to guide further exploration.

1. Introduction

Developing efficient sustainable energy conversion technologies is crucial for meeting global energy demands and tackling environmental issues.[1–4] Electrocatalysis plays an essential role in sustainable energy conversion systems,[5–8] including hydrogen evolution, ammonia production, and carbon dioxide conversion.[9–12] Although significant research has been conducted on these electrocatalytic reactions, there is still an

[a]State Key Laboratory of Flexible Electronics, Jiangsu Key Laboratory of Smart Biomaterials and Theranostic Technology, Institute of Advanced Materials (IAM), School of Chemistry and Life Sciences, Nanjing University of Posts and Telecommunications, Nanjing 210023, China. E-mail: iambchen@njupt.edu.cn; iamyhli@njupt.edu.cn

[b]Sustainable Energy and Environment Thrust, The Hong Kong University of Science and Technology (Guangzhou), Nansha, Guangzhou 511400, China. E-mail: qinbaiyun@hkust-gz.edu.cn

[c]Guangzhou HKUST Fok Ying Tung Research Institute, Nansha, Guangzhou, 511458, China

Bo Chen

Bo Chen received his B.S. degree, M.S. degree, and PhD degree from Lanzhou University (2009), Shandong University (2012), and Nanyang Technological University (2017), respectively. Then, he worked as a research fellow at Nanyang Technological University (2017–2020) before moving to the City University of Hong Kong as a research associate (2020–2023). Currently, he is a Professor at the School of Chemistry and Life Sciences, Nanjing University of Posts and Telecommunications. His current research interests include the synthesis, characterization, and applications of nanomaterials with unconventional phases.

Peiyu Duan

Peiyu Duan received her B.S. degree from Ludong University in 2024. She is currently pursuing her M.S. degree at the School of Chemistry and Life Sciences, Nanjing University of Posts and Telecommunications, under the supervision of Prof. Bo Chen. Her research interests include the synthesis of Cu-based intermetallics and their electrocatalytic applications.

urgent need for developing electrocatalysts with high activity, long-term stability, and low cost.

In recent years, extensive research on alloy catalysts has led to significant advancements in electrocatalytic reactions.[13–16] However, disordered alloys, despite their compositional diversity,[17] suffer from random atomic arrangements that lead to ambiguous relationships between their structure and performance, posing significant challenges for their practical applications.[18] This limitation stands in stark contrast to intermetallics with well-defined atomic arrangements, which endow them with superior physical and chemical properties.[19–21] The ordered structure in intermetallics enables uniform dispersion of active sites,[22] precise control over electronic structures,[23] remarkable stability,[24,25] and excellent activity,[26–28] making them highly attractive for various catalytic applications. Over the past few decades, these advantages have driven intermetallics to the forefront of catalyst research.[29–32]

Copper (Cu), a representative transition metal known for its excellent electrical conductivity,[33] facilitates efficient electron transport within catalytic systems. Its partially filled 3d orbital allows for orbital hybridization with other metals, resulting in bifunctional effects that can finely tune the local electronic environment. This modulation enhances the electronic density and activity of neighboring active sites, thereby improving the adsorption and utilization efficiency of key reaction intermediates.[34,35] Therefore, among various intermetallic systems, Cu-based intermetallics have received significant attention in electrocatalytic applications. By introducing other metal elements, the electronic structures and surface coordination environments of Cu-based intermetallics can be adjusted. For example, the incorporation of Zn can enhance water adsorption and dissociation, thereby providing active hydrogen sites. Thus, in Cu–Zn intermetallic systems, the spatial separation of active sites effectively modifies the adsorbed protonated species, promoting nitrite reduction to ammonia.[36] These merits highlight the potential of Cu-based intermetallics in energy conversion applications.

This review aims to provide a comprehensive summary of recent advancements in Cu-based intermetallics for electrocatalytic applications. It begins with a detailed classification of the structural configurations of Cu-based intermetallics and analysis of the thermodynamic and kinetic factors that influence their formation. Then, the synthesis techniques of Cu-based intermetallics are summarized, with an emphasis on strategies for optimizing their size and morphology. Moreover, the electrocatalytic applications of Cu-based intermetallics are systematically discussed, including the hydrogen evolution reaction (HER), oxygen reduction reaction (ORR), carbon dioxide reduction reaction (CO_2RR), and nitrate reduction reaction (NO_3RR). Finally, the challenges and potential future directions in this field are explored, offering insights into how these materials can be further developed for practical electrocatalytic applications.

2. Structures and components of Cu-based intermetallics

Compared with random alloys, intermetallics exhibit superior thermodynamic stability, higher activity, enhanced durability, and elevated resistance to dissolution. These properties arise from their precise stoichiometry and ordered atomic arrangement, which effectively suppress the diffusion and migration of metal atoms.[37] In this section, we discuss the structural characteristics and compositional diversity of Cu-based binary and multi-component intermetallics.

The various crystal structures of intermetallics are primarily derived from three types of monometallic structures: face-centered cubic (*fcc*), body-centered cubic (*bcc*), and hexagonal close-packed (*hcp*). As illustrated in Fig. 1, typical intermetallic structures derived from the *fcc* structure include $L1_0$ (CuAu-type,

Qinbai Yun

Qinbai Yun is currently an Assistant Professor in Sustainable Energy and Environment Thrust at The Hong Kong University of Science and Technology (Guangzhou). He obtained his B.E. and M.E. degrees from Tsinghua University, China, and then earned his PhD degree from Nanyang Technological University, Singapore, in 2020. After that, he worked as a Postdoc and Research Assistant Professor at the City University of Hong Kong and The Hong Kong University of Science and Technology, respectively. His research interests focus on the precise synthesis of low-dimensional metallic materials for applications in electrochemical energy conversion and electrocatalytic synthesis of fine chemicals.

Yonghua Li

Yonghua Li received his B.S. degree, M.S. degree, and PhD degree from Suzhou University (1998, 2001) and Nanjing University (2004) respectively. Then, he worked as a postdoctoral fellow at the National Institute of Advanced Industrial Science and Technology in Japan. Currently, he is a Professor at the School of Chemistry and Life Sciences, Nanjing University of Posts and Telecommunications. His current research interests include the synthesis, characterization, and applications of functional coordination compounds.

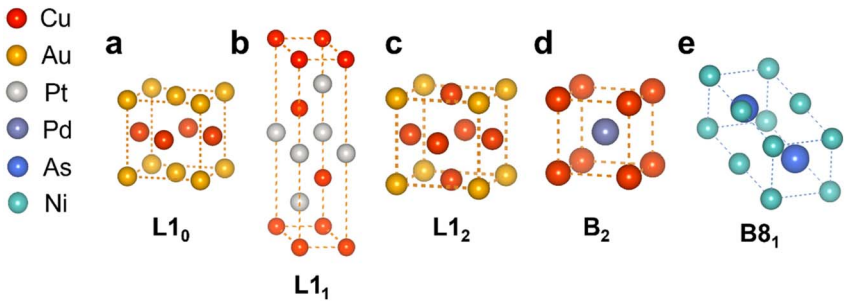

Fig. 1 Illustration of typical intermetallic structures. (a–c) *fcc*-derived intermetallic structures, including $L1_0$ (CuAu-type), $L1_1$ (CuPt-type), and $L1_2$ (Cu_3Au-type). (d) *bcc*-derived intermetallic structure B_2 (CuPd-type). (e) *hcp*-derived intermetallic structure $B8_1$.

space group *P*4/*mmm*), $L1_1$ (CuPt-type, space group $R\bar{3}m$), and $L1_2$ (Cu_3Au-type, space group $Pm\bar{3}m$). The $L1_0$ structure features a tetragonal distortion of the *fcc* lattice with alternately stacked atomic layers of two different elements at an atomic ratio of 1 : 1 along the *c*-axis. Although the $L1_2$ structure is derived from *fcc* as well, it contains two elements with an atomic ratio of 3 : 1, which are located at different sites within an *fcc* lattice. Typically, elements with higher atomic content occupy face-centered sites, while vertices are occupied by the other. Moreover, the *bcc*-derived B_2 structure (CsCl-type, space group $Pm\bar{3}m$) and *hcp*-derived $B8_1$ structure (NiAs-type, space group $P6_3/mmc$) are also commonly observed.[38]

2.1 Binary intermetallics

Binary intermetallic nanocatalysts, with precisely controlled shapes, sizes, and compositions, offer significant opportunities for improving catalytic activity and selectivity beyond their monometallic counterparts. These advantages primarily stem from synergistic or ensemble effects driven by electronic interactions between the hybridized atomic orbitals of different metals.[39]

2.1.1 Cu–Au intermetallics. According to previous research, common Cu–Au intermetallics include CuAu and Cu_3Au, whose crystal structure types are $L1_0$ and $L1_2$, respectively. In each unit cell, the atomic layer is located at a specific site, and Cu and Au atoms mainly occupy the positions of vertices or face centers at a certain ratio. In a recent study, Chen *et al.*[40] successfully synthesized an $L1_0$-phase CuAu intermetallic compound with a space group of *P*4/*mmm* (Fig. 1a). The molar ratio of Au : Cu was 1 : 1.02, and the average particle size was 5.60 nm, which was smaller than that of the *fcc* phase alloy. In particular, the lattice parameters (a = 3.968 Å, b = 3.968 Å, and c = 3.663 Å) also confirmed that the crystal structure changed compared to the standard *fcc* structure ($a = b = c$ = 3.954 Å). In addition, by tuning the appropriate Cu/Au ratio, Niu *et al.*[41] synthesized an $L1_2$ phase Cu_3Au intermetallic with ordered structures using Cu@Au core–shell nanowires as precursors. This $L1_2$ phase is based on *fcc* structures with long-range ordered atomic arrangements (Fig. 1c), where Cu atoms occupy face-centered positions, whereas Au atoms occupy top-corner positions. It is noteworthy that the $L1_2$ phase could be translated from the $L1_0$ phase during the synthesis of Cu–Au intermetallics. When heating the Cu@Au nanowires at progressively increased temperatures, the $L1_0$ phase first formed, which then transformed into the $L1_2$ phase.

2.1.2 Cu–Pt intermetallics. Cu–Pt intermetallics typically form CuPt ($L1_1$ phase) and Cu_3Pt ($L1_2$ phase) structures. Specifically, in the structure of $L1_2$, Cu atoms occupy face-centered positions, while Pt atoms occupy top-corner positions, similar to the atomic arrangement in Cu_3Au. However, because Pt has a larger atomic radius than Au, the lattice constant of Cu_3Pt is usually larger than that of Cu_3Au. For example, Jiang *et al.*[37] synthesized $L1_2$-$PtCu_3$/C intermetallic nanocrystals with a high ordering degree, which consisted of a $Pm\bar{3}m$ (221) space group. At the same time, Xing *et al.*[42] observed that the lattice parameter of Cu_3Pt was 5.288 Å, and it continued to decrease with increasing annealing temperature, whereas the lattice parameter of Cu_3Au was 3.74 Å at room temperature. Interestingly, when the atomic ratio of Cu to Pt is approximately 1 : 1, the resulting intermetallic CuPt forms a unique $L1_1$ phase structure. As shown in Fig. 1b, $L1_1$-CuPt is based on an *fcc* structure. Specifically, in its crystal structure, the (111) planes are alternately stacked with atomic planes composed solely of Cu atoms and those composed solely of Pt atoms. Each Pt atom is surrounded by a Cu atom, forming a long-range ordered atomic arrangement. Based on the work reported by Xu *et al.*,[43] the lattice parameter of the $L1_1$-phase CuPt typically ranges from 1.8961 to 1.9252 Å, and the exact value may vary slightly depending on the preparation method and experimental conditions.

2.1.3 Cu–Pd intermetallics. Notably, unlike the random CuPd solid solution with an *fcc* phase, CuPd intermetallics possess a CsCl-type (B_2) structure.[44] The B_2 phase belongs to the $Pm\bar{3}m$ space group, which is a cubic system with a high symmetry. This symmetry ensures that the structure is highly ordered and uniform. In this structure, Cu and Pd atoms occupy the apex and body center, respectively, similar to those of Cl and Cs in a bcc structure. For example, Cai *et al.*[45] achieved a disorder-to-order transformation from the A_1 (*fcc*) alloy phase of CuPd into the B_2 intermetallic phase through a wet-chemical approach. Interestingly, Zhai *et al.*[46] found that the atomic ratios of Cu/Pd were uncertain, changing between 1 and 2 depending on the temperature.

2.1.4 Cu–Sn intermetallics. Cu_3Sn and Cu_6Sn_5 are two common types of Cu–Sn intermetallics. Cu_3Sn can form various

crystal structures, including two orthorhombic structures, a hexagonal structure, and a cubic structure. The orthorhombic structures can exhibit different space groups, such as *Pmmn* and *Cmcm*,[47] with potentially different lattice parameters. The orthorhombic *Pmmn* structure has lattice parameters of a = 5.514 Å, b = 4.765 Å, and c = 4.329 Å. The *Cmcm* structure features a long-period superlattice with extended dimensions on the *b*-axis, with lattice parameters of a = 5.516–5.529 Å, b = 47.75–48.79 Å, and c = 4.323–4.342 Å.[48,49] The hexagonal structure ($P6_3/mmc$) has lattice parameters of a = 2.752 Å, and c = 4.322 Å. The cubic structure ($Fm\bar{3}m$) has a lattice parameter of a = 5.514 Å. Additionally, Cu_6Sn_5 can form various crystal structures, including hexagonal and monoclinic systems. The hexagonal (η-Cu_6Sn_5) structure has a NiAs/Ni_2In-type ($B8_1/B8_2$ type, Fig. 1e) structure,[50] where Cu atoms randomly occupy the trigonal bipyramidal sites formed by Sn atoms, with lattice parameters of a = 4.07 Å, and c = 4.63 Å. The monoclinic (η′-Cu_6Sn_5) structure has a more ordered arrangement of Cu atoms and vacancies, forming a monoclinic structure with lattice parameters of a = 12.21 Å, b = 4.07 Å, c = 4.63 Å, and β = 90.0°.

2.1.5 Other binary intermetallics. Cu atoms have a partially filled electronic structure of [Ar] $3d^{10}4s^1$, which endows them with high chemical reactivity, enabling them to react with a variety of metal elements to form diverse intermetallics. Previous studies have found that metals from Group IIIA often serve as secondary metals, forming intermetallics with Cu atoms. Much research has focused on the formation of Cu–Al intermetallic compounds. The dominant intermetallic phases, AlCu, Al_2Cu, and Al_4Cu_9,[51,52] exhibit orthorhombic, tetragonal, and primitive cubic structures, respectively. Wan *et al.*[53] synthesized monolithic nanoporous $Cu_{11}In_9$/Cu and observed a representative $Cu_{11}In_9$/Cu interfacial region using high-resolution transmission electron microscopy (HRTEM). The monoclinic intermetallic $Cu_{11}In_9$ phase and *fcc* Cu matrix can be identified using fast Fourier transform (FFT) patterns. Moreover, Bagchi *et al.*[54] synthesized intermetallic $CuGa_2$ (tetragonal system, space group $P4/mmm$) and Cu_9Ga_4 (cubic phase, space group $P\bar{4}3m$). The crystal structure of $CuGa_2$ consists of alternating layers of Cu (1D sheet) and Ga (square net), while $CuGa_2$ has the same centrosymmetric space group ($P4/mmm$) as quasi-2D α-$FeSi_2$ or LiFeAs with $d_{Cu-Cu} = a$ = 2.83 Å and an interplanar distance of c = 5.839 Å.

2.2 Multi-component intermetallics

2.2.1 High-entropy intermetallics (HEIs). High-entropy alloys (HEAs) consist of five or more metal elements, with the atomic percentage of each element ranging from 5 at% to 35 at%.[55] Attributing to the high-entropy configuration, different atoms randomly or nearly randomly occupy various positions in the lattice during the formation of HEAs, thus resulting in the lack of long-range chemical ordering.[56] Despite their complex compositions, HEAs generally form simple solid-solution phases (*e.g.*, *fcc*, *bcc*, and *hcp*).[57,58] However, HEIs combine the characteristics of HEAs and intermetallics, possessing the advantages of multi-metal high-entropy effects and an ordered atomic structure. They can provide more uniformly isolated[59] and highly efficient active sites and thus have received extensive attention and research in recent years. For example, Wang *et al.*[60] prepared PtRuFeNiCu HEIs with a typical *fcc* structure. The XRD pattern showed (100) and (110) superlattice diffraction peaks of the ordered intermetallic phase, indicating the successful formation of the HEI structure. In another case, Wang *et al.*[61] synthesized $Pt_4FeCoCuNi$ HEIs, and the characterization indicated that the intermetallic compound had an $L1_0$ ordered structure.

2.2.2 Heterostructured intermetallics. Heterostructured intermetallics typically consist of two or more different types of intermetallics. This structural design not only retains the unique properties of each component but also generates new synergistic effects through interfacial interactions. Nanomaterials with heterogeneous structures and multiple components are important for the development of next-generation functional materials and have great potential for various applications. The structure of each component and the interface between them determine the properties of heterostructured nanomaterials.[62] Wang *et al.*[63] prepared CuSn catalysts by electrochemically depositing Sn nanoparticles onto Cu foam and then annealed the samples at 300 °C for 3 h in a nitrogen atmosphere to form heterostructured Cu_3Sn/Cu_6Sn_5 intermetallics. According to the XRD analysis, upon annealing, the diffraction pattern of Sn disappeared and a new peak emerged at 30.1°, which was attributed to the (221) plane of Cu_6Sn_5, along with three additional peaks at 37.7°, 41.7°, and 57.5°, which were assigned to the (002), (110), and (200) planes of Cu_3Sn, respectively, suggesting the formation of an intermetallic heterostructure. The heterostructured intermetallic integrates the properties of Cu_3Sn and Cu_6Sn_5, thereby enhancing their performance in electrocatalytic applications.

3. Growth mechanisms of Cu-based intermetallics, including kinetic and thermodynamic analysis

Thermodynamic and kinetic discussions are necessary to gain a deeper understanding of the growth behavior of intermetallics. Thermodynamic analysis predicts the stability and feasibility of intermetallic formation, while kinetic analysis provides insights into the reaction rate and mechanisms. By combining these analyses, researchers can gain a deeper understanding of the factors influencing intermetallic growth, which is essential for optimizing the structure and performance of Cu-based intermetallics.

3.1 Thermodynamic analysis

The second law of thermodynamics is often employed to predict the thermodynamic trend of the formation of intermetallics, thereby enhancing the possibility of successful synthesis and selectivity for ordered structures. The Gibbs free energy change (ΔG) for the mixing process of bimetallic systems can be expressed as eqn (1):

$$\Delta G = \Delta H - T\Delta S \quad (1)$$

ΔH is the enthalpy change during the formation of intermetallics, ΔS is the entropy change, and T is the absolute temperature. The formation of intermetallics is accompanied by an increase in the strength of the intermetallic bond and an increase in the degree of atomic ordering; thus, ΔH and ΔS are both negative. Also, eqn (1) reveals the Gibbs free energy change for the transition of the system from a disordered alloy to an ordered intermetallic. As shown in Fig. 2, when the other variables of the system are the same, the enthalpy change becomes the main contributing term at low temperatures, and the interatomic bonding is strong, thus favoring the transition from a disordered solid solution to an ordered intermetallic phase, while at high temperatures, the entropy of the disordered phase is higher, and the entropy-related term ($T\Delta S$) dominates in the total free energy, thus favoring the transition from order to disorder.

However, in the actual synthesis process, the change of surface free energy becomes a non-negligible part of the total Gibbs free energy when the size of the material reduces to the nanoscale.[64] Therefore, eqn (1) is supplemented by introducing a third term for the change in Gibbs free energy caused by the change in surface area, as shown in eqn (2):[65]

$$\Delta G' = \Delta H - T\Delta S + \Delta\gamma A \quad (2)$$

where T is the absolute temperature, $\Delta\gamma$ is the change in surface free energy, and A is the surface area. After the formation of intermetallics, the average bonding energy on the surface of the ordered phase is higher than that on the surface of the disordered phase, so $\Delta\gamma$ is positive. It is worth noting that $\Delta\gamma$, ΔH, and ΔS are all determined by the intrinsic properties of the bimetallic system, such as the components, morphology, and state of the precursors, whereas the adjustment of experimental conditions can modulate T and A. Based on the assumption that the shape remains constant during the mixing process (A is constant), the relationship between the transition temperatures of intermetallic nanomaterials and bulk materials is explored,[66] as shown in eqn (3), where ΔH_v is the specific heat by volume and is negative with the same sign as ΔH. The specific surface area A/V is inversely proportional to the size of the nanocrystals and decreases with increasing nanocrystal size. Therefore, smaller nanocrystals usually require lower temperatures for the transition from a disordered to an ordered phase.

$$T_{nano}/T_{bulk} = 1 + (A/V)\,\Delta\gamma/\Delta H_v \quad (3)$$

As a transition metal element, Cu has 3d electrons that can hybridize with the d electrons of other transition metal atoms, forming strong d–d orbital interactions. This strong orbital hybridization enhances the chemical bond strength between atoms, which in turn releases more energy during the formation of intermetallics, resulting in a more negative ΔH value. This interaction provides part of the enthalpy change for the transition from disordered alloys to ordered intermetallics, which in turn reduces the Gibbs free energy of the intermetallic formation process and promotes its formation.[67]

In recent years, high-entropy intermetallics have received increasing attention. These compounds are characterized by multi-element mixing and slow elemental diffusion, leading to the formation of high-entropy atomic configurations.[68] In this system, the contribution of entropy changes to the total Gibbs free energy becomes more pronounced, thereby further enhancing the thermodynamic driving force for the formation of intermetallics. This phenomenon provides new concepts and directions for the synthesis and design of intermetallics.

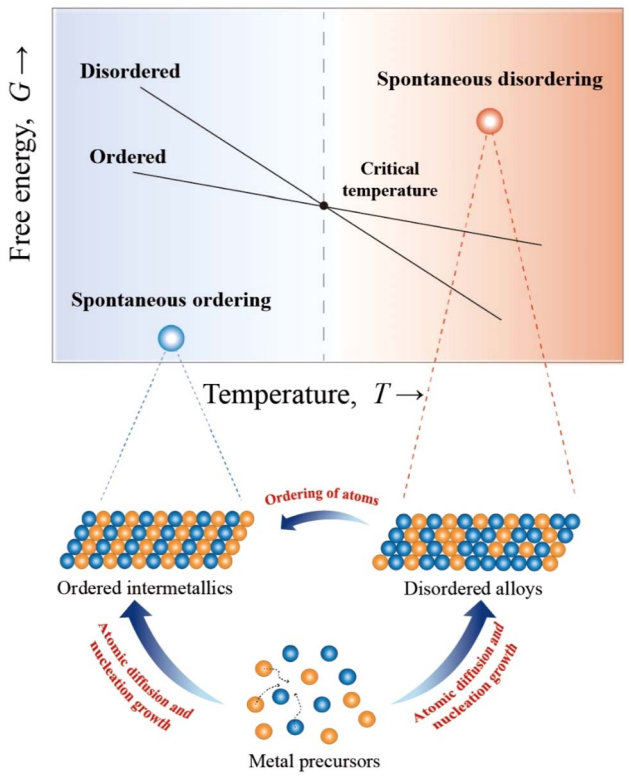

Fig. 2 Thermodynamic tendencies of bi-metallic systems at different temperatures.

3.2 Kinetic analysis

Compared to thermodynamics, kinetic driving forces are more dominant in the synthesis of intermetallics, but the influencing factors to be considered are more complex. In general, both the nucleation process of new phases and the diffusion process of atoms can be analyzed.

The classical Johnson–Mehl–Avrami–Kolmogorov (JMAK) theory is used to explain the nucleation and growth processes of the new phase, and an equation for the transformation fraction from a disordered to an ordered state has been proposed.[69] In eqn (4),[70] f represents the conversion rate, N is the nucleation rate, v is the growth rate, and t is the reaction time. The conversion rate f follows an S-curve law, where the growth rate is slower in the initial state and near the completion of the reaction, while in the intermediate process, nanocrystals grow at a very fast rate.

$$f = 1 - \exp(-\pi/3Nv^3t^n) \quad (4)$$

The atomic diffusion is a process in which metal atoms continuously promote local atomic rearrangement by successively jumping to neighboring positions in the lattice. The Arrhenius equation can be used to describe atomic mobility as shown in eqn (5),[65,71] where D_0 is the diffusion front factor, which depends on the effects of various factors such as the bond strength, atomic type, and effective mass of the selected metal precursor. The atomic migration activation energy E_{diff} refers to the energy potential generated by metal atoms jumping from one position to another. R is the ideal gas constant, and T is the absolute temperature.

$$D = D_0 \exp(-E_{diff}/RT) \quad (5)$$

As shown in Fig. 3, in the early stages of intermetallic formation, there are high diffusion barriers and strong metallic bonds in the rigid lattice, so large kinetic energy barriers need to be overcome to form thermodynamically stable intermetallic phases. In addition, according to the expression for the nucleation work W^* shown in eqn (6),[66] the interfacial free energy change is positive and a size effect occurs. Here, W^* represents the total energy barrier for nucleation, which includes the ΔG and the interfacial energy contribution ($\Delta\gamma A$). As the size continues to decrease, the specific surface area increases dramatically, leading to a decrease in the kinetic driving force of small nanocrystals. In addition, in the process of converting disordered alloys into ordered intermetallics, the interfacial energy generated by the new phases can act as an energy barrier to subsequent transformations. Together, these three factors constitute a major kinetic barrier to diffusion.

$$W^* = \Delta G + \Delta\gamma A \quad (6)$$

Therefore, it is necessary to adopt strategies to enhance the kinetic driving force by artificially altering the external energy or introducing defects or vacancies in the original metal system. On the one hand, thermal activation strategies can be adopted by increasing the annealing temperature during the reaction process. This approach can promote the generation of vacancies/defects and increase the atomic migration rate. However, it is crucial to prevent crystal agglomeration caused by excessive temperatures. On the other hand, introducing defects into the solid solution precursor system can provide additional jump sites for atomic diffusion, thereby effectively increasing the kinetic driving force. Notably, in the Cu–Au binary metal system, the defect formation energy and jump potential energy of the weakly bonded atoms are relatively low,[72] thus making it easier to overcome the barrier potential and synthesize the desired intermetallics.

In summary, we explored the possibility of intermetallic synthesis from a thermodynamic point of view and analyzed the driving force problem of the reaction from a kinetic point of view, thus providing a preliminary understanding of the formation of intermetallics. In the next section, we will discuss common synthesis methods and key influencing factors in the synthesis process.

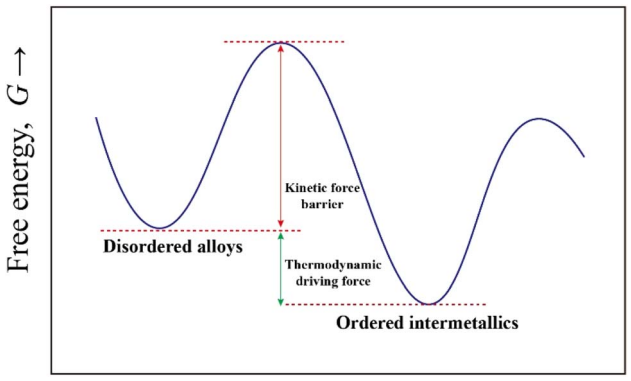

Fig. 3 Energy changes from disordered alloys to ordered intermetallics.

4. Synthetic methods of Cu-based intermetallics

There are various methods for synthesizing Cu-based intermetallics, among which the most commonly used are thermal annealing and liquid-phase synthesis. Thermal annealing involves heating a material to a specific temperature and then cooling it slowly to achieve the desired structures. In recent years, to address the issue of nanocrystal agglomeration during the thermal annealing process, a series of methods, such as support-assisted annealing and protective shell-assisted annealing, have been proposed. In contrast, liquid-phase synthesis can precisely control the size and shape of nanomaterials in a low-temperature environment, resulting in products with good dispersion, low energy consumption, and short reaction time. Therefore, selecting an appropriate synthesis method is crucial for obtaining Cu-based intermetallics with desired structures.

4.1 Thermal annealing

4.1.1 Direct annealing. As one of the most widely used methods for preparing Cu-based intermetallics, the direct annealing method usually transforms disordered solid precursors such as Cu-based alloys or core–shell structures into ordered intermetallics by thermal annealing in H_2, Ar and other atmospheres or a vacuum.[66,73] For example, Niu *et al.*[41] converted the liquid-phase synthesized Cu@Au core–shell nanowires into atomically ordered Cu_3Au intermetallic nanowires by annealing them at different temperatures (140 to 320 °C) for 1 h in an H_2/Ar mixture atmosphere (H_2/Ar: 10/90). The annealing temperature significantly influenced the phase transformation and atomic ordering processes. Specifically, at temperatures below 200 °C, the Cu@Au nanowires exhibited a mixture of Cu and Au phases with partial mixing, as indicated by the appearance of a broad peak assigned to the A_1 Cu–Au (111) reflection in the XRD pattern. When the annealing temperature increased to 220 °C, a drastic phase transition from tetragonal CuAu ($L1_0$ phase) to cubic Cu_3Au ($L1_2$ phase) occurred. At higher temperatures (≥240 °C), the atomic diffusion continued, leading to the formation of fully ordered Cu_3Au nanowires. This

study also demonstrated that the presence of twin boundaries in Cu@Au nanowires facilitated the ordering process at relatively low temperatures.

4.1.2 Support-assisted annealing. The direct annealing method can solve the problems of low atomic mobility and a relatively high kinetic barrier in solid compounds by using relatively high annealing temperatures and long annealing times. However, the formation of intermetallics during high-temperature annealing causes the aggregation of nanocrystals, Oswald ripening, and/or sintering, resulting in increased particle size and thus deteriorating the electrocatalytic performance of Cu-based intermetallics. To solve this problem, a support-assisted annealing method, in which materials are deposited on a suitable and stable carrier and then subjected to annealing, is proposed to inhibit the agglomeration of nanocrystals that may occur during annealing by the anchoring effect. At present, the common carriers used to immobilize nanocrystals include carbon black, C_3N_4, porous carbon, oxides, *etc.*[70,74] Through this strategy, Chen *et al.*[40] loaded $CuCl_2$ and $HAuCl_4 \cdot 3H_2O$ precursors onto activated Ketjen black *via* a modified co-precipitation method, and the obtained product was annealed at different temperatures (200 to 600 °C) in an atmosphere of 5% H_2 and 95% Ar to form ordered and disordered AuCu/C with different crystal structures (Fig. 4a). The XRD patterns of AuCu/C formed by annealing at different temperatures (Fig. 4b) show that the sample annealed at 200 °C exhibits only the (111) and (200) peaks, indicating a disordered structure. When the annealing temperature reached 300 °C, (001) and (110) superlattice peaks began to appear, indicating a transition from a disordered to an ordered crystal structure. Simultaneously, as the temperature increased, the particle size gradually increased, and the degree of structural ordering changed, resulting in the intensity of the superlattice peak first increasing and then decreasing. Arumugam *et al.* used Ketjen black as a carrier to prepare *fct*-PtFeCu/C. The metal precursor mixed with Ketjen black was annealed at 800 °C in an H_2/N_2 atmosphere to form an ordered intermetallic.[77] In another study, according to the process shown in Fig. 4c, Peng *et al.*[75] dispersed Cu and Mg powders on carbon black and annealed them at 700 °C for 4 h in a H_2/Ar ($\nu_{H_2} : \nu_{Ar} = 5\% : 95\%$) atmosphere. The use of carbon black as a carrier can limit the aggregation and size increase of particles and induce the preferential growth of the Cu_2Mg (111) crystal plane to form a Cu_2Mg intermetallic with (111) crystal plane orientation. Fig. 4d shows that the XRD pattern of Cu_2Mg (111) (red curve in Fig. 4d) aligns well with that of the standard Cu_2Mg structure with the *Fd3m* space group. At the same time, the difference of the intensity ratios of (111) to (311) peaks (I_{111}/I_{311}) of Cu_2Mg (111) and the traditional CuMg alloy (blue curve in Fig. 4d) proves the preferred crystal plane growth in Cu_2Mg (111). Subsequent experiments showed that the Cu_2Mg intermetallic prepared by support-assisted annealing exhibited better electrocatalytic performance than the traditional CuMg alloy in the electroreduction of CO_2 to ethanol. In addition to using carbon black as the carrier during the annealing process, urea was introduced by Jiang *et al.* during the synthesis of a $PtCu_3$

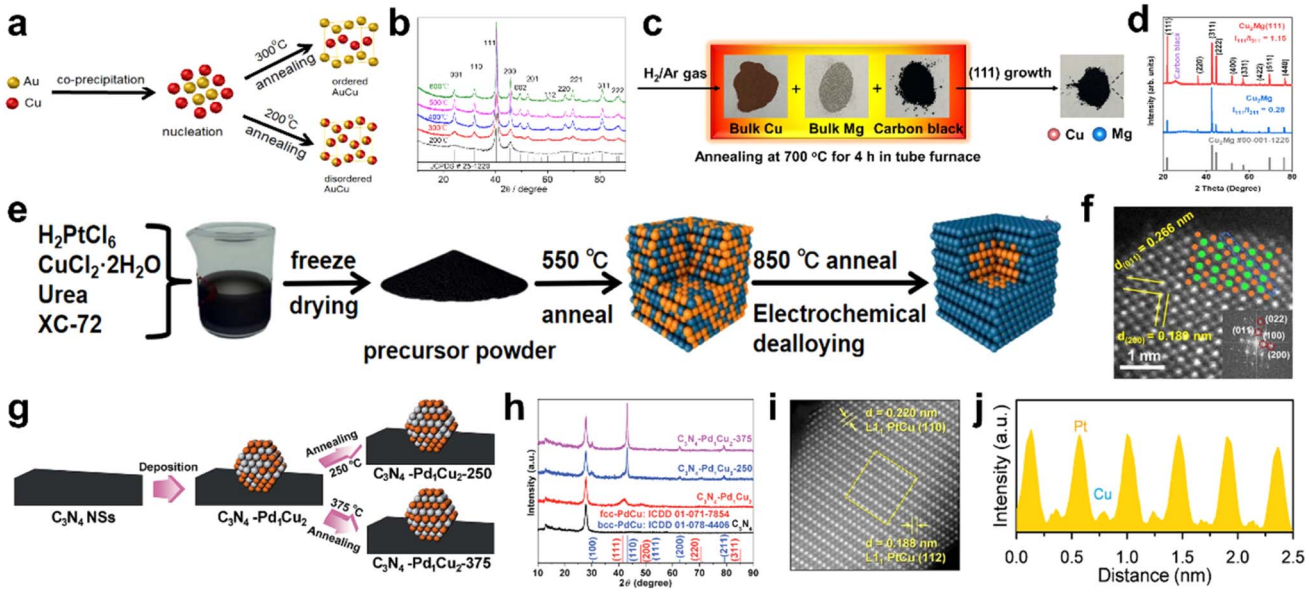

Fig. 4 (a) Schematic diagram of the preparation of ordered and disordered AuCu/C. (b) XRD patterns of AuCu/C nanoparticles annealed at 200 to 600 °C.[40] Reproduced with permission. Copyright 2017 The Electrochemical Society. (c) Schematic diagram for the synthesis of Cu_2Mg intermetallic nanocrystals. (d) XRD patterns of nano Cu_2Mg (red curve) and conventional Cu_2Mg (blue curve).[75] Reproduced with permission. Copyright 2024 Wiley-VCH. (e) Schematic illustration of the preparation of $L1_2$-$PtCu_3$/C. (f) Enlarged HAADF-STEM image of $L1_2$-$PtCu_3$/C. Inset: the corresponding FFT image.[37] Reproduced with permission. Copyright 2024 The Royal Society of Chemistry. (g) Schematic illustration of the synthesis and (h) XRD patterns of C_3N_4–Pd_1Cu_2, C_3N_4–Pd_1Cu_2-250 and C_3N_4–Pd_1Cu_2-375.[45] Reproduced with permission. Copyright 2018 The Royal Society of Chemistry. (i) Magnified HAADF-STEM image of O–PtCuNF/C and (j) Z-contrast intensity profile taken from the dashed yellow area in (i).[76] Reproduced with permission. Copyright 2020 American Chemical Society.

intermetallic with an $L1_2$ ordered structure to suppress the particle size growth (Fig. 4e).[37] The aberration-corrected high-angle annular dark-field scanning transmission electron microscopy (HAADF-STEM) image (Fig. 4f) shows that the Pt atoms (green) and Cu atoms (orange) are alternately arranged. Simultaneously, superlattice spots can be observed in the fast Fourier transform (FFT) pattern, proving the atomically ordered intermetallic structure.

In addition, C_3N_4 can also be used as a carrier to prepare Cu-based intermetallics. For example, Cai *et al.*[45] deposited PdCu alloy nanoparticles on C_3N_4 nanosheets and annealed them at 250 and 375 °C for 1 h in an atmosphere of 5% H_2/95% N_2 to form C_3N_4–Pd_1Cu_2-250 and C_3N_4–Pd_1Cu_2-375, respectively (Fig. 4g). As shown in the XRD patterns (Fig. 4h), the peak of the A_1 phase in C_3N_4–Pd_1Cu_2-250 becomes weaker and a new peak appears, which corresponds to the ordered *bcc* phase of PdCu, indicating that the originally disordered Pd_1Cu_2 nanocrystals have been partially transformed into ordered structures. When the annealing temperature reaches 375 °C, the peak corresponding to the B_2 phase of C_3N_4–Pd_1Cu_2-375 becomes stronger and the peak of the A_1 phase disappears, proving that the disordered PdCu alloy has been completely transformed into ordered PdCu intermetallic nanocrystals. Owing to the strong electrostatic interaction between PdCu and C_3N_4, Pd_1Cu_2 nanoparticles have higher stability on C_3N_4. Thus, in addition to electron transfer, C_3N_4 nanosheets can effectively inhibit the aggregation of Pd_1Cu_2.

4.1.3 Protective shell-assisted annealing. Shell-assisted annealing inhibits the diffusion and aggregation of nanoparticles by forming a protective shell on their surface, thereby accurately controlling the particle size of nanocrystals. In general, metal oxides and polymers are often used as protective coatings.[70,74] For example, Kim *et al.*[76] used silica as a protective shell to mediate annealing, washed the annealed powder with a 1 wt% HF solution to remove the silica protective layer, and finally obtained PtCu nanoframes with an atomically ordered intermetallic structure (O–PtCuNF/C). The ordered arrangement of atoms in the HAADF-STEM image of O–PtCuNF/C (Fig. 4i) and the periodic distribution of Pt and Cu atoms in the Z-contrast intensity profile (Fig. 4j) can confirm the ordered arrangement of atoms in the PtCuNF/C intermetallics. It should be noted that while coating a protective shell during the annealing process is effective in preventing the nanoparticles from sintering and agglomerating, how to remove the protective shell in the subsequent treatment and expose the surface of the nanocrystals to achieve high catalytic performance is an issue worth considering.[70,74]

4.2 Liquid-phase synthesis methods

As mentioned in the previous section, nanocrystal aggregation/sintering needs to be addressed in the preparation of Cu-based intermetallics by thermal annealing. In contrast, liquid-phase synthesis is usually achieved at relatively low temperatures. The use of surfactants can also alleviate the agglomeration of nanomaterials to a certain extent. At the same time, liquid-phase synthesis can regulate the structure and composition of the synthesized intermetallics by adjusting various parameters such as solvents, reducing agents, capping agents, and surfactants, which are of great significance for the fields of synthesis and catalysis.[66,78,79]

4.2.1 One-pot synthesis. One-pot synthesis refers to the addition of metal precursors, solvents, reducing agents, surfactants and other chemicals in a container to achieve a reaction equilibrium under relatively mild conditions, where ordered intermetallic nanomaterials with a certain size and shape can form (Fig. 5a). In general, when the reduction potentials of different metals vary greatly, the use of strong reducing agents such as ascorbic acid (AA), tetrabutylammonium bromide (TBAB), $NaBH_4$, and *n*-butyllithium can effectively achieve the co-reduction of metal precursors.[66,78] In a typical example, Gao *et al.*[80] added copper(II) acetylacetoacetate ($Cu(acac)_2$) and $PdCl_2$ as precursors, oleylamine (OAm) as a solvent and reducing agent, and trioctylphosphine (TOP) as a surfactant in a three-necked flask to synthesize CuPd intermetallics. From the HAADF-STEM image in Fig. 5b, the ordered atomic arrangement can be observed in CuPd nanocrystals, while the corresponding FFT pattern (inset of Fig. 5b) and the atomic model overlay in Fig. 5c show the cubic structure of nanocrystals. Xia *et al.*[82] also used OAm as a reducing agent to prepare $PtCu_3$ nanocages, in which OAm played the roles of solvent, reducing agent and stabilizer at the same time. In addition, by increasing the amount of cetyltrimethylammonium bromide (CTAB), which served as a stabilizer and structure-directing agent, nanocrystals became uniformly dispersed and gradually transformed from concave solid nanoparticles into cage-like structures. However, when the amount of CTAB reached 150 mg, the nanocages were coated with excess CTAB, resulting in crystal aggregation. Therefore, the addition of an appropriate amount of CTAB was beneficial for the formation and dispersion of $PtCu_3$ nanocages. It is noteworthy that in one-pot synthesis, the addition of halide ions can coordinate with metal precursors, thereby significantly reducing the reaction rate. Meanwhile, halide ions can also promote the local oxidative etching of defective nanoparticles to form defect-free single crystals with low surface energies.[83] For instance, Mathiesen *et al.*[84] added a certain amount of AA and $FeCl_3$ in the reaction solution to synthesize PdCu intermetallic nanoparticles, and the Fe^{3+}/Fe^{2+} pair introduced by $FeCl_3$ as an effective and controllable etching source can synergistically promote oxidative etching, and Cl^- can coordinate with metal ions. Simultaneously, AA, as a strong reducing agent, can increase the reduction rate of metal ions. The combination of these two additives can effectively control the morphology and structure of the product and finally form the ordered PdCu intermetallic.

4.2.2 Seed-mediated synthesis. Although the huge differences in reduction potentials between different metal elements can be overcome by using strong reducing agents to a certain extent, it is still difficult to form nanocrystals with well-defined structures because such structures need to grow in a mild reducing environment. The seed-mediated method, by (i) forming nanocrystal seeds with well-defined sizes and shapes containing one or more components and (ii) diffusion of

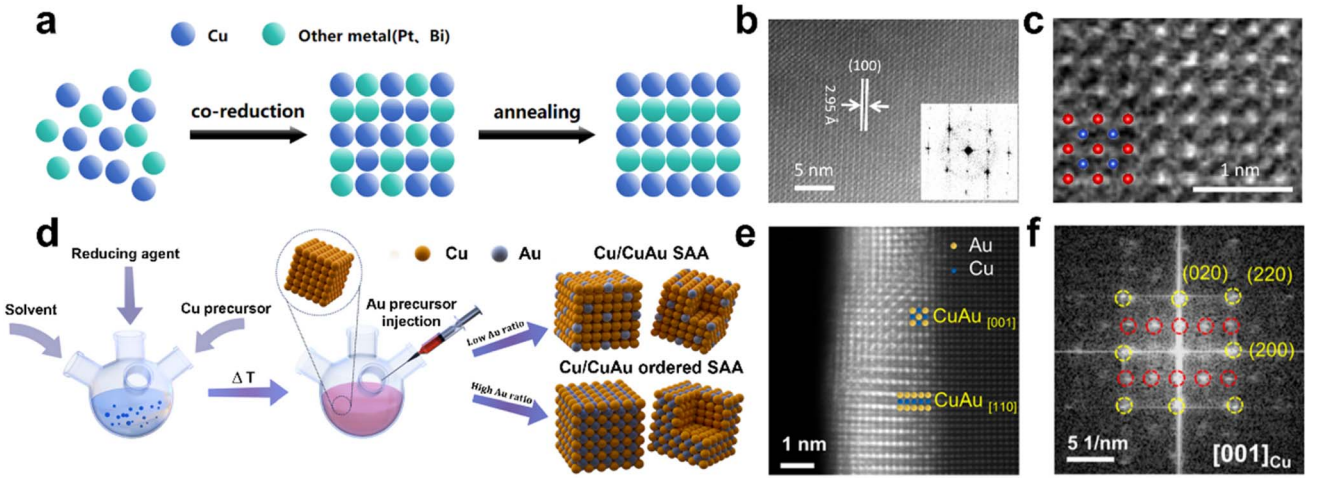

Fig. 5 (a) Schematic illustration of one-pot synthesis of Cu-based intermetallics. (b) HAADF-STEM image of the ordered CuPd nanocube. The inset shows the corresponding FFT pattern of the CuPd nanocube. (c) Enlarged HAADF-STEM image of the ordered CuPd nanocubes. The blue and red balls represent Cu and Pd atoms, respectively.[80] Reproduced with permission. Copyright 2022 Springer Nature. (d) Schematic illustration of the synthesis of core/shell Cu/CuAu SAA. (e) Atomic-resolution HAADF-STEM image and (f) the corresponding FFT pattern of a Cu/CuAu ordered SAA nanocube.[81] Reproduced with permission. Copyright 2023 Springer Nature.

a second metal into the pre-formed seeds under specific conditions, can form intermetallics with well-defined sizes, shapes, compositions, and crystal structures.[66,78,79] Using this method, Gao *et al.*[81] synthesized core/shell Cu/CuAu single-atom alloys (SAAs) with an ordered monoatomic intermetallic layer. As shown in Fig. 5d, the solvent, reducing agent, and copper precursor were first added to a three-neck flask to generate a slightly red solution containing Cu nanocubes by the co-reduction method and then Au precursor was injected drop-by-drop, thus allowing Au to diffuse instantaneously to the surface of Cu nanocrystals. When the Au content was low, only disordered Cu/CuAu SAAs can be generated, while a high Au content would lead to the formation of ordered Cu/CuAu SAAs. From the HAADF-STEM image (Fig. 5e) and the corresponding FFT image (Fig. 5f), it can be seen that the synthesized ordered Cu/CuAu SAA nanocubes have a tetragonal *P*4/*mmm* intermetallic structure. In another example, Clarysse *et al.*[85] also prepared a red dispersion solution of Cu seeds by adding Cu precursors, OAm, and tri-*n*-octylphosphine oxide (TOPO) into a three-necked flask, followed by rapid injection of the Ga precursor to form Cu–Ga intermetallic nanocrystals. However, the seed-mediated method also suffers from the cumbersome preparation processes. Moreover, synthesis at a relatively low temperature may have insufficient driving force to overcome the activation barrier, thus forming a partially ordered intermetallic structure. However, the well-defined structures and adjustable structural parameters of intermetallics prepared *via* the seed-mediated method also provide advantages that cannot be ignored. Therefore, the seed-mediated method is still an effective and promising method for the controlled preparation of intermetallics with well-defined structures.[78,79]

Beyond the conventional synthetic approaches, electrochemical deposition has emerged as another effective strategy for fabricating Cu-based intermetallics. Under an applied electric field, ionic species in the electrolyte migrate toward the electrodes, where redox reactions occur, enabling the controlled formation of target catalyst materials. For instance, Deng *et al.*[32] designed an electrolyte containing optimized concentrations of Cu^{2+} and Zn^{2+} ions and successfully synthesized $Cu_{100}Zn_{4.9}$ intermetallics on the working electrode surface *via* a one-step co-electrodeposition process. This method offers a low-energy, straightforward, and efficient route for producing high-performance Cu-based intermetallic electrocatalysts.

4.3 Key factors for preparing Cu-based intermetallics

4.3.1 Metal additives. The introduction of additional metals into alloys or intermetallics modulates thermodynamic and kinetic driving forces, thus affecting the growth behavior of intermetallics. Common metal additives include Ni,[86] Ag,[87,88] Zn,[89] *etc.* For example, many studies have verified that the addition of Ni has a significant effect on the structure of Cu-based intermetallics. In a study reported by Sun *et al.*,[90] it was found that the addition of Ni resulted in a unique bimodal structure, which synergized with the highly conductive Cu substrate to significantly improve the electron transfer efficiency and electrolyte accessibility. However, in the Cu–Sn intermetallic, the addition of Ni led to a change in the intermetallic morphology. For example, Gao *et al.*[91] investigated the effect of Ni addition on the growth behavior of intermetallics. They found that the addition of Ni led to the formation of a new $(Cu, Ni)_6Sn_5$ phase, which inhibited the diffusion of the substrate Cu atoms and led to a morphological change of Cu_6Sn_5 from the original fan-shaped structure to a flat structure. Moreover, the study by Zhang *et al.*[92] revealed a similar phenomenon. The addition of a trace amount of Ni inhibited the growth of the intermetallic, whereas sufficient Ni could promote the growth of the intermetallic layer when the Ni content was 10%.

4.3.2 Elemental ratios. Different ratios of metal precursors can have distinct effects on the growth of intermetallics. On the one hand, different ratios of metal elements can improve the selectivity of the products and result in different intermetallics. For example, in the work reported by Chen *et al.*,[72] the selective synthesis of CuAu and Cu_3Au was successfully achieved by choosing different ratios of raw materials. However, on the other hand, when the concentrations of metal elements deviate from the optimal ratios, atomic aggregation will occur, leading to an uneven distribution of elements, which results in disordered alloying of the products.

4.3.3 Temperature. Temperature is an important factor in enhancing the kinetic driving force, facilitating atomic diffusion and nucleation processes, thus increasing the growth rate of intermetallics. For example, Peng *et al.*[93] compared the growth kinetics of Cu–Sn intermetallics at different temperatures. Both theoretical predictions and experimental results demonstrated that an increase in temperature favored the diffusion of atoms, resulting in a significant increase in the consumption rate of Sn precursors, thus promoting the growth of Cu_6Sn_5 and Cu_3Sn intermetallics.

4.4 Particle size and morphology control

The Ostwald ripening effect, which occurs during the high-temperature annealing process, may lead to the aggregation and sintering of nanocrystals. Consequently, it is essential to explore suitable reaction conditions to regulate the size and morphology of the synthesized intermetallics.

4.4.1 Strategies for particle size control of intermetallics. The size effect on the growth behavior of intermetallics can also be analyzed both thermodynamically and kinetically. In the thermodynamic analysis, according to eqn (3), where $\Delta\gamma$ is positive and ΔH_v is negative, the continuous decrease in nanocrystal size leads to a significant increase in the specific surface area, resulting in an augmentation of the A/V ratio. Consequently, smaller nanocrystals require lower transition temperatures for their formation.[78]

The kinetic analysis, however, presents a more intricate scenario with two opposing effects. On one hand, as crystal size diminishes, the distances between metal atoms shorten, reducing the diffusion paths and enhancing the diffusion rates, thereby lowering the diffusion barriers. On the other hand, according to the kinetic discussion on diffusion barriers, the increase in specific surface area leads to an increase in the total Gibbs free energy owing to the positive $\Delta\gamma$, which in turn increases the nucleation work, significantly hindering the driving force for the nucleation process. In summary, for small nanocrystals, the detrimental effect on the driving force prevails, whereas for large bulk crystals, the sluggish diffusion rate becomes the dominant impediment.

Therefore, optimizing the synthesis conditions and regulating the size range, that is most conducive to the growth of intermetallics, are crucial to balance these competing factors and achieve optimal synthesis outcomes. The optimization can be approached in two ways: by increasing the distance between nanocrystals or employing stronger chemical forces to eliminate agglomeration.[74] Some effective methods such as support-assisted annealing, protective shell-assisted annealing, and wet-chemical synthesis have been proposed for particle size control, which have been discussed in detail in the previous sections.

4.4.2 Strategies for morphology control of intermetallics. Crystals with different morphologies expose different crystal facets and thus have different specific surface areas. So thermodynamically and kinetically, this is considered in a similar way to the size effect previously described, resulting in changes in the specific surface area and surface free energy. Therefore, according to eqn (2), different crystal facets have different surface free energies, leading to variations in the driving force for energy of reaction processes on the surface (such as adsorption, reactions, *etc.*). In addition, the states and diffusion path of electrons on the surface can also vary depending on the specific exposed crystal facets.[94]

In order to prevent the destruction of the initial crystal structure during the annealing process, two key considerations are proposed to maintain the shape of the alloy precursor while allowing the phase transition: constructing a robust original structure or lowering annealing/reaction temperatures.[66] Therefore, a number of methods have been developed including protective shell-assisted annealing and hard template methods, as mentioned previously.

5. Electrocatalytic applications of Cu-based intermetallics

Through precise control and optimization of the local structures and electronic properties of active sites, the catalytic activity and selectivity of Cu-based intermetallics can be significantly enhanced.[95] Their long-range ordered crystal structures also endow them with high structural stability during electrocatalytic processes. Therefore, in recent years, Cu-based intermetallics have shown excellent performance toward various electrocatalytic reactions, such as the HER, ORR, CO_2RR, and NO_3RR (Table 1).

5.1 Hydrogen evolution reaction

Hydrogen, as an emerging renewable and clean energy carrier, shows great potential for replacing conventional fossil fuels. Hydrogen production *via* water electrolysis provides a practical path for sustainable development by efficiently converting renewable electrical energy into hydrogen. The simplified equation for the HER as the cathodic reaction of water electrolysis can be expressed as the following eqn (7):[101]

$$2H_3O^+ + 2e^- = H_2 + 2H_2O \text{ (in acid) or } 2H_2O + 2e^- = H_2 + 2OH^- \text{ (in alkaline)} \quad (7)$$

Conventional electrocatalysts often use noble metals such as Pd and Pt as main catalysts,[102] which are costly and scarce and have poor stability in aqueous solutions, leading to material loss and reduced durability. In contrast, Cu doping can effectively reduce the usage of noble metals and realize the

Table 1 Examples of the application of Cu-based intermetallics in the field of electrocatalysis

Cu-based intermetallics	Synthetic methods	Electrocatalytic applications	Reference
PdCu	Electrochemical treatment	HER	96
$Pt_4FeCoCuNi$	One-pot synthesis	HER	61
$AuCu_3$	Other liquid-phase synthesis	ORR	97
PtCu	Support-assisted annealing	ORR	76
AuCu	Support-assisted annealing	CO_2RR	98
$CuGa_2$	Support-assisted annealing	CO_2RR	54
Cu_9Ga_4	Direct annealing	CO_2RR	99
Cu_2Mg	Support-assisted annealing	CO_2RR	75
PdCu	Support-assisted annealing	NO_3RR	100
PdCu	One-pot synthesis	NO_3RR	80

synergistic catalytic effects. Cu-based intermetallics exhibit higher activity and better stability in the HER due to their tunable surface structure and active site distribution. Flores Espinosa *et al.*[96] synthesized a PdCu intermetallic and demonstrated that its enhanced catalytic activity stemmed from structural transformation from the PdCu random alloy (PdCu-A_1) into the intermetallic B_2 phase, as evidenced by the HER polarization curves (Fig. 6a). The PdCu-B_2 intermetallic structure exhibited a smaller Tafel slope (27 mV dec^{-1}) and lower overpotential in an acidic environment (Fig. 6b). Specifically, it only required an overpotential of 19.7 mV, which was much lower than that of Pd nanowires (231.2 mV) and comparable to that of commercial Pt/C (19.2 mV). Moreover, the catalyst exhibited excellent performance in alkaline environments. Density-functional theory (DFT) calculations further revealed that the improved HER performance of the PdCu–B_2 intermetallic can be attributed to the reduced hydrogen bonding energy (HBE) and the low water dissociation energy (E^aH_2O), which was only second to that of Pt (Fig. 6c and d), thus facilitating hydrogen adsorption and accelerating proton transfer.

In addition to binary intermetallics, high-entropy intermetallics have demonstrated unique advantages in catalysis in recent years due to their ordered structures and diverse components. Wang *et al.*[61] reported $Pt_4FeCoCuNi$ high-entropy intermetallic, which not only optimized the electronic structure but also improved the water dissociation capacity, thus facilitating the alkaline HER process. Electrocatalytic measurements showed that its mass activity was 5.6 times higher than that of commercial Pt/C (Fig. 6e) and it had lower overpotentials and Tafel slopes (Fig. 6f), indicating a high HER activity. Moreover, multi-element mixing and slow atomic diffusion endowed high-entropy intermetallics with excellent durability, and the catalytic activity did not undergo significant reduction after the 50-h HER stability test.

5.2 Oxygen reduction reaction

Besides the HER, the ORR is another critical process in energy conversion technologies, particularly in fuel cells, and its reaction process can be expressed as follows:[103]

$$O_2 + 4e^- + 4H^+ = 2H_2O \text{ (in acid) or}$$
$$O_2 + 4e^- + 2H_2O = 4OH^- \text{ (in alkaline)} \quad (8)$$

It has been reported that Cu can significantly enhance the extent of O–O bond cleavage by reducing the energy barrier for the formation of the O_2^* intermediate, as well as optimizing the release of *OH. This effectively promotes the activation process of O_2. Thus, Cu-based intermetallics greatly accelerate ORR kinetics and exhibit good catalytic activity. Specifically, an $AuCu_3$ intermetallic with the non-precious metal Cu as the catalytic center was reported by Zhang *et al.*[97] The intermetallic exhibited excellent catalytic performance in alkaline environments, with half-wave potentials comparable to those of commercial Pt/C and mass current densities 1.5 times higher than those of Pt/C. DFT calculations verified that this excellent ORR performance was attributed to the bimetallic synergism between Cu and Au, in which Cu contributed to the activation of O_2 molecules, making Cu-based intermetallics have great potential for ORR catalysts.

In addition to Au, Cu-based intermetallics formed by the introduction of other metals, such as Pt and Cu, also exhibit good catalytic performance. Kim *et al.*[76] reported a PtCu intermetallic (Fig. 7a and b), which exhibited a very high ORR activity owing to the enhanced strain and ligand effect. From the cyclic voltammetry curves of the catalyst (Fig. 7c), it can be seen that the ordered PtCu intermetallic (O–PtCuNF/C) has a lower OH_{ad} peak current density, suggesting that it has more abundant OH_{ad} active sites on the surface, thus favoring OH^- adsorption. Compared with the disordered alloy structure, the O–PtCuNF/C catalyst had a higher mass activity, reaching 2.1 times that of the disordered alloy (D-PtCuNF/C), and still maintained a good mass activity after 10 000 cycles (Fig. 7d), demonstrating excellent stability.

The excellent ORR performance of the PtCu intermetallic was also reported in the recent study by Deng *et al.*[104] Linear scanning voltammetry (LSV) was used to evaluate the electrochemical performances of catalysts (Fig. 7e), which showed that all PtCu catalysts outperformed the pure Pt/C catalyst, and the ordered structure of the PtCu intermetallic played an important role in improving the ORR activity. After 50 000 cycles, the activity of the ordered PtCu/hollow mesoporous carbon sphere (O–PtCu/HMCS) catalysts underwent a certain degree of attenuation, but the mass activity was still superior to those of the control samples and other state-of-the-art ORR catalysts. Here, it is worth mentioning that carbon materials, such as HMCS,

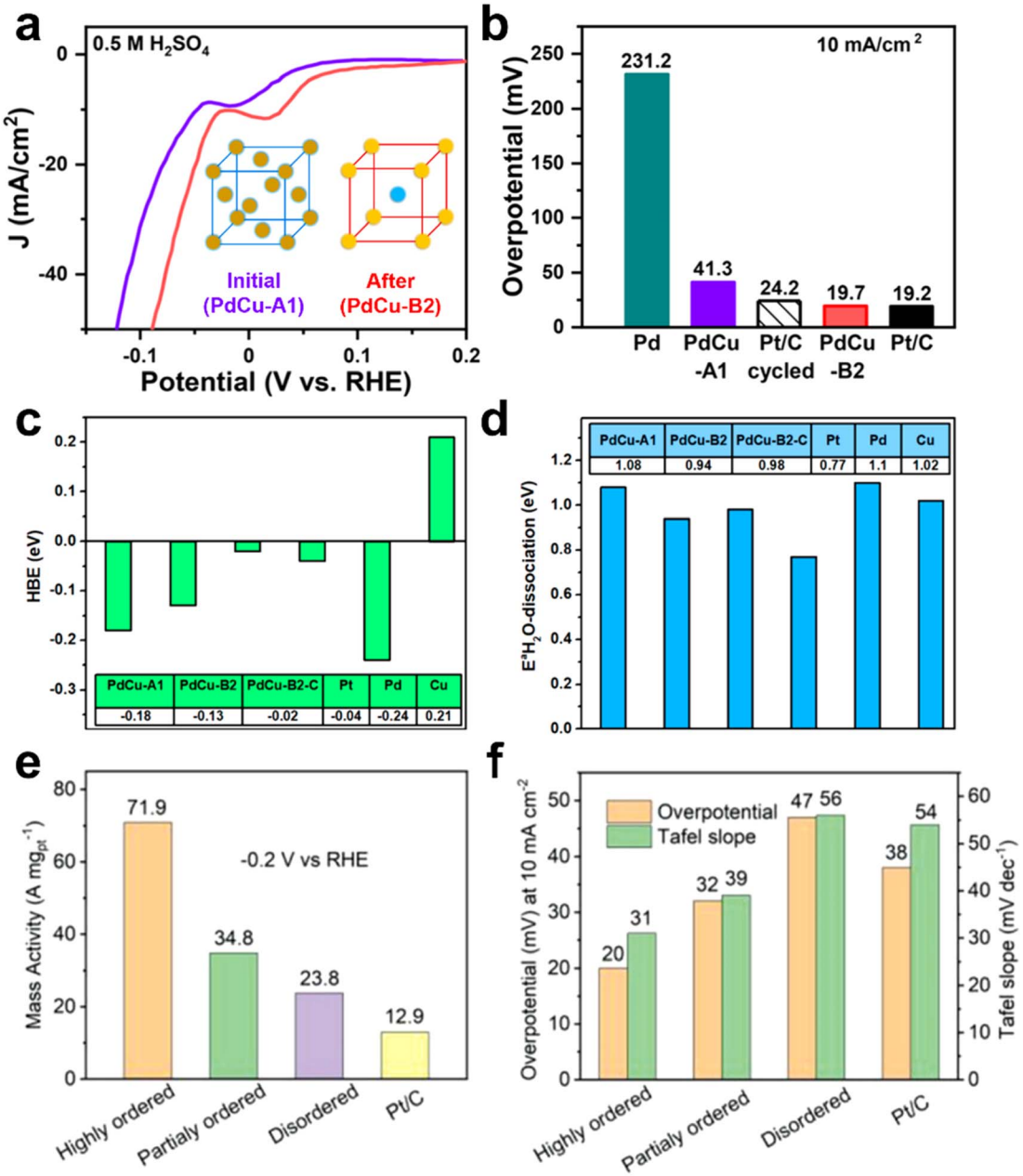

Fig. 6 (a) Polarization curves of PdCu intermetallics for the HER (purple and red lines represent the initial disordered alloy state and the ordered intermetallic state at a later stage of the reaction, respectively). (b) Comparison of overpotentials of different catalysts. (c and d) DFT calculations of HBEs (c) and $E^{a}H_2O$ (d) for the PdCu–B_2 intermetallic and other catalysts.[96] Reproduced with permission. Copyright 2020 American Chemical Society. (e and f) Comparison of mass activities at −0.2 V *vs.* RHE (e), Tafel slopes and overpotentials (f) for $Pt_4FeCoCuNi$ with different ordering degrees and commercial Pt/C.[61] Reproduced with permission. Copyright 2023 Wiley-VCH.

can be used as ideal supports to promote catalytic reactions due to their high surface area and good structural permeability.[105]

5.3 CO_2 reduction reaction

The continuous increase in the atmospheric CO_2 concentration resulting from rapid industrialization has become an urgent environmental problem. In this background, the CO_2RR has attracted much attention due to its ability to convert CO_2 into value-added chemicals or fuels by utilizing renewable electrical energy. Cu exhibits moderate adsorption energy for key CO_2RR intermediates, which optimizes the binding strength and enhances the catalytic activity of Cu-based intermetallics.[106] Notably, due to its unique electronic structure and adsorption properties, Cu is the only metal catalyst that can efficiently and selectively produce multi-carbon (C_{2+}) products (such as ethylene, ethanol, and propanol) in the CO_2RR.[107–109]

The bimetallic synergistic effect promotes the optimization of CO_2RR kinetics when Cu forms an ordered intermetallic structure with other metals, such as Au. Cu–Au intermetallics

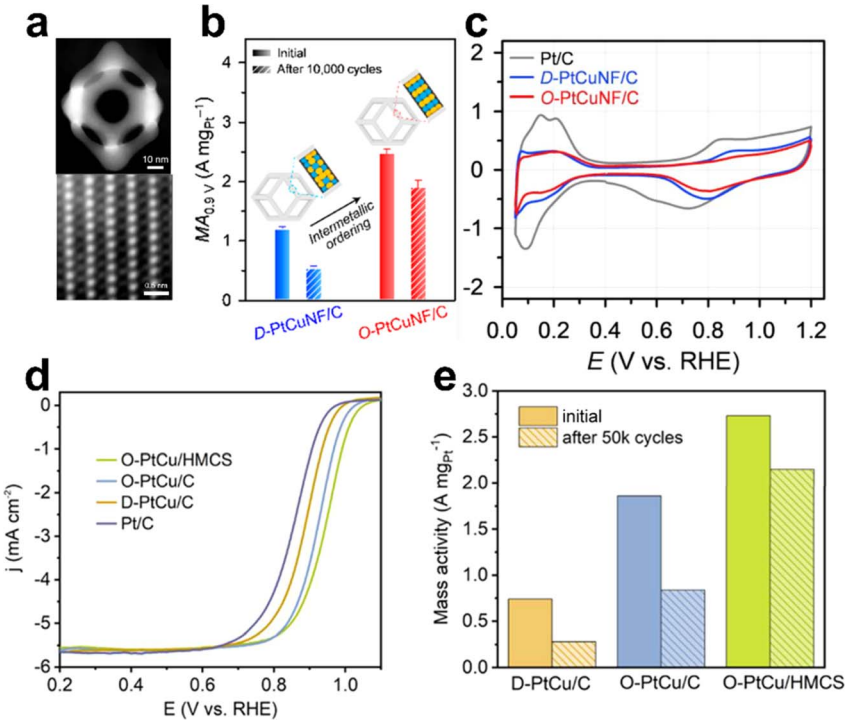

Fig. 7 (a) HAADF-STEM image of O–PtCuNF/C. (b) Comparison of initial mass activities and those after 10 000 cycles of O–PtCuNF/C and disordered PtCu (D-PtCu)NF/C at −0.9 V. (c) Cyclic voltammograms of O–PtCuNF/C, D-PtCuNF/C and Pt/C.[76] Reproduced with permission. Copyright 2020 American Chemical Society. (d) LSV curves and (e) changes in mass activity before and after 50 000 cycles for O–PtCu/HMCS and controlled samples.[104] Reproduced with permission. Copyright 2024 American Chemical Society.

exhibit excellent stability in the CO_2RR due to the high enthalpy of mixing and strong atomic interactions between Cu and Au atoms.[110] For example, Han *et al.*[98] reported that an AuCu intermetallic catalyst could successfully achieve efficient catalytic generation of CO, and the corresponding catalytic mechanism diagram is shown in Fig. 8a. The electrocatalytic test results showed that the catalyst with an intermetallic structure had a smaller Tafel slope of approximately 106 mV dec^{-1} (Fig. 8b) and a Faraday efficiency (FE) of up to 75% toward CO (Fig. 8c), indicating that the HER was effectively suppressed and thus a high CO selectivity was achieved.

In addition to the selective generation of CO, Cu-based intermetallics have shown excellent catalytic activity in the catalytic generation of other C_1 products, such as CH_3OH. Bagchi *et al.*[54] synthesized a $CuGa_2$ intermetallic as a CO_2RR electrocatalyst, and the FE for the selective conversion of CO_2 to methanol on $CuGa_2$ could reach up to 77.26% at a potential of −0.3 V *vs.* RHE.

By further rationally modulating the configurations of active sites, it is possible to synthesize an ordered structure with Cu interspaced with Ga atoms, where the active *CO binding sites are uniformly distributed. This can significantly change the surface adsorption behavior and effectively increase the coverage of *CO, thereby enhancing the selectivities of C_2 products. Yan *et al.*[99] successfully prepared a Cu_9Ga_4 intermetallic with high catalytic activity and selectivity for the production of various C_2 products (such as ethylene and ethanol). Specifically, this catalyst achieved a partial current density of 1207 mA cm^{-2} for C_2 products and a corresponding FE of up to 71%.

It is noteworthy that, unlike the studies mentioned above, Peng *et al.*[75] expanded the scope of the second metal to the alkaline earth metal Mg and reported a Cu_2Mg electrocatalyst, which also exhibited excellent catalytic activity for the generation of ethanol. As illustrated in Fig. 8d, the (111) facet of the Cu_2Mg intermetallic features a dense arrangement of Cu_3 and Cu_6 ring structures, which significantly lowers both the energy barrier and reaction energy for the rate-determining *CO–CO coupling step (Fig. 8e). The Mg atoms are uniformly embedded within the lattice, effectively modifying the coordination environment of the Cu active centers. This structural configuration enhances the surface coverage of *CO intermediates and stabilizes the *CHCHOH species, thereby markedly improving the selectivity for CO_2 reduction toward ethanol production. As shown in Fig. 8f, the FE of ethanol can reach up to 76.2%, although the product contains small amounts of CH_4 and C_2H_4 in addition to C_2H_5OH and CO, and the corresponding partial current density of C_2H_5OH can reach up to 720 mA cm^{-2} (Fig. 8g). This work provides a brand-new strategy for the high-efficiency synthesis of ethanol by the CO_2RR.

5.4 Nitrate reduction reaction

Nitrates, as common pollutants in human industrial and agricultural wastewater, pose a significant threat to the ecological balance of water bodies and severely endanger human health.[111] At the same time, ammonia, as a key raw material, has a wide range of applications in various fields,

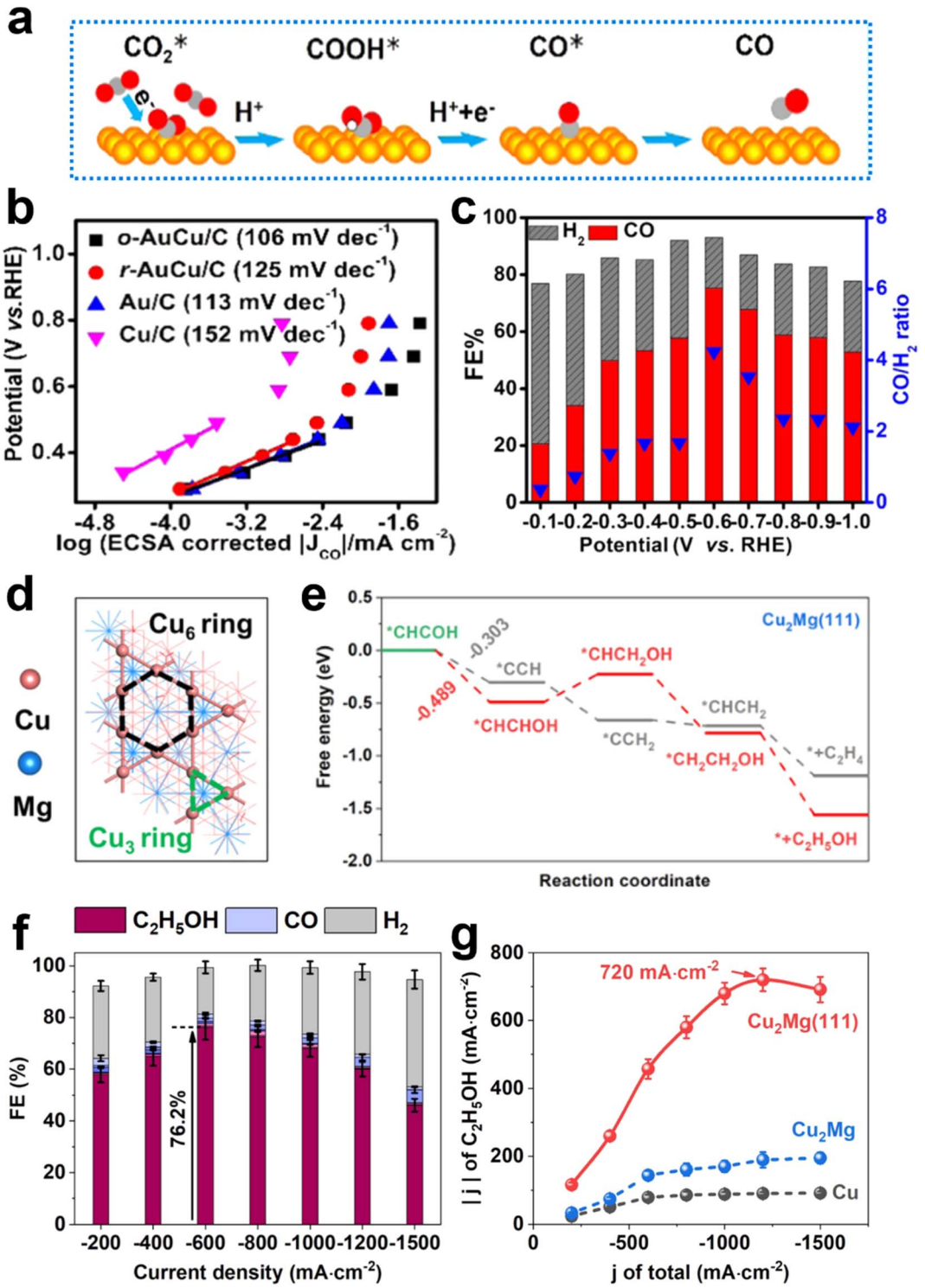

Fig. 8 (a) The catalytic mechanism of the CO_2RR on the AuCu catalyst. (b) Comparison of Tafel slopes of ordered the AuCu intermetallic (o-AuCu/C), a random AuCu alloy (r-AuCu/C), Au/C and Cu/C. (c) The FEs of CO and H_2 products for the o-AuCu catalyst.[98] Reproduced with permission. Copyright 2021 American Chemical Society. (d) The top view of the Cu_2Mg (111) model, composed of Cu_3 and Cu_6 rings, with Mg atoms orderly arranged. (e) The free energy diagram for the conversion of the *CHCOH intermediate to ethanol and ethylene on the Cu_2Mg (111) surface. (f) FEs of products at different potentials on Cu_2Mg (111). (g) Comparison of partial current densities for C_2H_5OH on different catalysts.[75] Reproduced with permission. Copyright 2024 Wiley-VCH.

such as fertilizer production, chemical manufacturing, and fuel development. However, traditional synthesis methods, such as the Haber–Bosch process, are energy-consuming and costly; meanwhile, the NO_3^- produced by the Ostwald process may lead to secondary pollution problems in the environment.[112] In view of this, the NO_3RR has been widely studied in

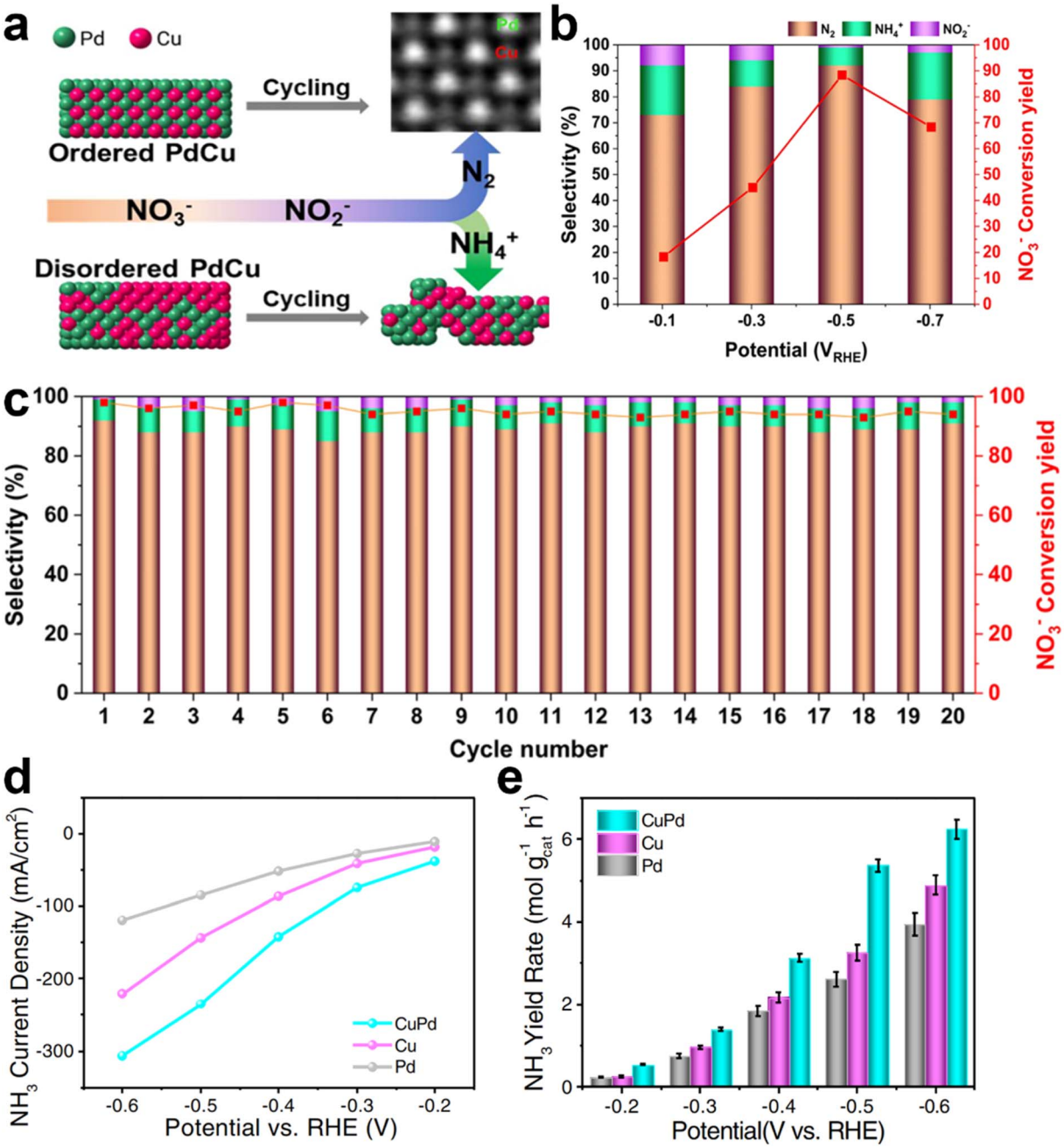

Fig. 9 (a) Differences in product selectivity between ordered and disordered PdCu. (b) NO_3^- conversion rate and N_2/NH_4^+ selectivity of ordered PtCu. (c) Stability test of ordered PtCu.[100] Reproduced with permission. Copyright 2023 American Chemical Society. (d) Partial current densities of NH_3 and (e) NH_3 yield at different potentials for ordered CuPd, Cu and Pd.[80] Reproduced with permission. Copyright 2022 Springer Nature.

recent years[113] and utilizes electrons as a reducing agent to achieve efficient transformation of nitrates in wastewater, and in some cases, it can convert nitrates into NH_3 products with high added value.

Cu exhibits a strong adsorption capacity for NO_3^- due to its unique partially filled electronic structure, which can effectively promote the reduction of NO_3^- to NO_2^- and NO, accelerate the formation of N–H, and inhibit the HER effectively, thus making Cu a highly active NO_3RR catalyst in neutral and alkaline media.[114–116] In order to further enhance the stability and catalytic performance of Cu, combining it with other metals to form intermetallics becomes an important route. In a study reported by Lim *et al.*,[100] it was confirmed that the ordered PdCu intermetallic exhibited a selectivity of 91% for the production of N_2, much better than that of the disordered alloy (44% for N_2 and 49% for NH_4^+), achieving almost complete removal of NO_3^- at the optimum potential (Fig. 9a and b). In addition, the NO_3^- conversion and N_2 selectivity remained at a high and stable level after 20 cycles (Fig. 9c), further validating its excellent catalytic performance and stability.

In addition, Gao *et al.*[80] employed interpretable machine learning to successfully predict and synthesize CuPd intermetallic nanomaterials. The electrocatalytic results showed that the catalyst has a high NH_3 partial current density (Fig. 9d), with FE up to 92.5%, and an NH_3 yield of up to 6.25 mol h^{-1} g^{-1} at a potential of −0.6 V (Fig. 9e), providing an interpretable machine-learning-assisted structure prediction strategy.

5.5 Other electrocatalytic applications

In addition to the electrocatalytic applications discussed above, Cu-based intermetallics have also shown good performance in the methanol oxidation reaction (MOR) and ethanol oxidation reaction (EOR). For example, Zhou *et al.*[117] prepared a surface-modified PtCu intermetallic, which was able to increase the enrichment level of hydroxyl groups and ethanol and accelerate the cleavage of the C–C bond in ethanol. The electrocatalytic test results showed that its mass activity could reach 17.83 A mg_{Pt}^{-1} and the selectivity for CO_2 was 93.5%, which was 30 times that of Pt/C, demonstrating excellent EOR performance. Furthermore, in a research study published by Xing *et al.*,[42] the binary intermetallic formed by Pt and Cu also exhibited good MOR performance, delivering a high specific activity of 3.23 mA cm^{-2} and a mass activity of 1200 mA mg_{Pt}^{-1}. Notably, a recent study by Lan *et al.*[32] reported the successful synthesis of a series of Cu–Zn intermetallics that exhibit outstanding performance in the electrochemical conversion of nitrite to ammonia. The catalysts achieved a remarkable FE of up to 95% for NH_3 production and demonstrated long-term operational stability over 220 hours at a high current density of 500 mA cm^{-2}. This work presents a promising strategy for advancing Cu-based intermetallics in electrocatalytic ammonia synthesis.

6. Conclusion and outlook

This review summarizes the recent progress in Cu-based intermetallics, focusing on their structural characteristics, synthesis techniques, and electrocatalytic applications. The crystal structures of these materials are examined, along with the discussion of the thermodynamic and kinetic factors influencing their formation. Subsequently, a range of synthetic methods, especially thermal annealing and liquid-phase synthesis, are presented. Moreover, the electrocatalytic applications of Cu-based intermetallics in the HER, ORR, CO_2RR, and NO_3RR are demonstrated. Although Cu-based intermetallics present these promising advantages, their practical applications are still impeded by several unresolved challenges. Based on the current achievements, we propose several key directions for future research:

Barriers to scale-up production. Despite the significant advancements in the preparation of Cu-based intermetallics, their scale-up production still faces several obstacles, including susceptibility to oxidation, difficulties in morphological regulation, and uncontrolled aggregation due to high annealing temperatures. These factors contribute to Ostwald ripening, leading to nanocrystal aggregation and reduced exposure of catalytically active sites. Addressing these issues requires a deeper understanding of the thermodynamic and kinetic principles underlying the synthesis processes.

Clarifying structure–performance relationships. Although DFT calculations have shed light on how reaction intermediates interact with the Cu surface,[118] a deeper understanding of the structure–performance relationships between the structures of Cu-based intermetallics and their catalytic properties is still needed. Molecular dynamics simulations, for example, could provide valuable insights into atomic migration and diffusion, enabling the design of stable and well-dispersed materials.[119,120] Future work should leverage *in situ* characterization techniques and computational tools to reveal the electronic and atomic arrangements within different lattice structures and their influence on electrocatalytic performance. Advancing theoretical models and using machine learning to optimize design strategies could facilitate the creation of Cu-based intermetallics with precisely modulated properties.

Advancing phase engineering. Research on Cu-based intermetallics mainly focuses on traditional thermodynamically stable phases, with limited attention paid to unconventional metastable phases. As known, the crystal phase is an important structural parameter of materials.[121] Different crystal structures can exhibit different physical and chemical properties. By altering the arrangement of atoms,[122] metastable unconventional phases can be synthesized,[123,124] which exhibit excellent electrocatalytic properties. Therefore, in recent years, crystal phase engineering has been widely studied.[125] Building on these discoveries, future studies could focus on integrating intermetallic compounds with phase engineering to further explore their unique structural and electronic characteristics and apply them in electrocatalysis and other applications.

In summary, addressing the above challenges through a combination of experimental and computational approaches is crucial for the advancement of Cu-based intermetallics. By optimizing synthesis processes, deepening the understanding of structure–property relationships, and exploring novel phases, this field can unlock new possibilities for energy conversion and other emerging applications.

Conflicts of interest

There are no conflicts to declare.

Acknowledgements

This work was financially supported by the Key Grant for Special Professors in Jiangsu Province (RK119STP23002), the Natural Science Research Start-up Foundation of Recruiting Talents of the Nanjing University of Posts and Telecommunications (NY223016), 2024 Nanjing Science and Technology Innovation Program (NJKCZYZZ2024-06), the Project of State Key Laboratory of Organic Electronics and Information Displays, Nanjing University of Posts and Telecommunications (No. ZS030ZR24004 and ZS030ZR23034), and the Guangdong Basic and Applied Basic Research Foundation (No. 2023A1515110010 and 2024A1515012653).

References

1 X. Yin, R. Yang, G. Tan and S. Fan, *Science*, 2020, **370**, 786–791.
2 Z. Yao, Y. Lum, A. Johnston, L. M. Mejia-Mendoza, X. Zhou, Y. Wen, A. Aspuru-Guzik, E. H. Sargent and Z. W. Seh, *Nat. Rev. Mater.*, 2023, **8**, 202–215.
3 Q. Hassan, S. Algburi, A. Z. Sameen, H. M. Salman and M. Jaszczur, *Int. J. Hydrogen Energy*, 2024, **50**, 310–333.
4 L. Tang, H. Peng, J. Kang, H. Chen, M. Zhang, Y. Liu, D. H. Kim, Y. Liu and Z. Lin, *Chem. Soc. Rev.*, 2024, **53**, 4877–4925.
5 H. Kim, J. M. Kim, G. T. Park, Y. J. Ahn, J. Y. Hwang, D. Aurbach and Y. K. Sun, *Adv. Energy Mater.*, 2024, **15**, 2403386.
6 J. Li, X. Meng, X. Song, J. Qi, F. Liu, X. Xiao, Y. Du, G. Xu, Z. Jiang, S. Ye, S. Huang and J. Qiu, *Adv. Funct. Mater.*, 2024, **34**, 2316718.
7 S. Jia, L. Wu, L. Xu, X. Sun and B. Han, *Ind. Chem. Mater.*, 2023, **1**, 93–105.
8 Y. Ma, X. Meng, K. Li, L. Zhang, Y. Du, X. Cai and J. Qiu, *ACS Catal.*, 2023, **13**, 1290–1298.
9 J. Masa, C. Andronescu and W. Schuhmann, *Angew. Chem., Int. Ed.*, 2020, **59**, 15298–15312.
10 Z. Masaud, G. Liu, L. E. Roseng and K. Wang, *Chem. Eng. J.*, 2023, **475**, 145882.
11 N. Govindarajan, G. Kastlunger, H. H. Heenen and K. Chan, *Chem. Sci.*, 2022, **13**, 14–26.
12 Z. W. Seh, J. Kibsgaard, C. F. Dickens, I. B. Chorkendorff, J. K. Norskov and T. F. Jaramillo, *Science*, 2017, **355**, eaad4998.
13 R. Wu, X. Liu, Z. Li, S. Li, H. Zhu, H. Zhong, H. Wang, Y. Wu, S. Jiang, X. Zhang, X. Wang and Z. Lu, *Acta Mater.*, 2025, **284**, 120644.
14 J. Li, L. Li, X. Ma, J. Wang, J. Zhao, Y. Zhang, R. He, Y. Yang, A. Cabot and Y. Zhu, *Nano Res.*, 2024, **17**, 2328–2336.
15 L. Meng, C.-W. Kao, Z. Wang, J. Ma, P. Huang, N. Zhao, X. Zheng, M. Peng, Y.-R. Lu and Y. Tan, *Nat. Commun.*, 2024, **15**, 5999.
16 L. Zhang, H. Hu, C. Sun, D. Xiao, H.-T. Wang, Y. Xiao, S. Zhao, K. H. Chen, W.-X. Lin, Y.-C. Shao, X. Wang, C.-W. Pao and L. Han, *Nat. Commun.*, 2024, **15**, 7179.
17 P. Zhang, S. Hong, N. Song, Z. Han, F. Ge, G. Dai, H. Dong and C. Li, *Chin. Chem. Lett.*, 2024, **35**, 109073.
18 E. Antolini, *Appl. Catal., B*, 2017, **217**, 201–213.
19 S. Furukawa and T. Komatsu, *ACS Catal.*, 2017, **7**, 735–765.
20 Z. Qi, C. Xiao, C. Liu, T. W. Goh, L. Zhou, R. Maligal-Ganesh, Y. Pei, X. Li, L. A. Curtiss and W. Huang, *J. Am. Chem. Soc.*, 2017, **139**, 4762–4768.
21 Y. Yang and M. Wei, *J. Mater. Chem. A*, 2020, **8**, 2207–2221.
22 Z. Jia, T. Yang, L. Sun, Y. Zhao, W. Li, J. Luan, F. Lyu, L. C. Zhang, J. J. Kruzic, J. J. Kai, J. Huang, J. Lu and C. T. Liu, *Adv. Mater.*, 2020, **32**, 2000385.
23 L. Rößner and M. Armbrüster, *ACS Catal.*, 2019, **9**, 2018–2062.
24 C. Ma, H. Zhang, J. Xia, X. Zhu, K. Qu, F. Feng, S. Han, C. He, X. Ma, G. Lin, W. Cao, X. Meng, L. Zhu, Y. Yu, A.-L. Wang and Q. Lu, *J. Am. Chem. Soc.*, 2024, **146**, 20069–20079.
25 Y. Zhu, X. Wang, L. Feng, R. Zhao, C. Yu, Y. Liu, Y. Xie, B. Liu, Y. Zhou and P. Yang, *Nat. Commun.*, 2024, **15**, 8696.
26 T. Gunji, S. H. Noh, F. Ando, T. Tanabe, B. Han, T. Ohsaka and F. Matsumoto, *J. Mater. Chem. A*, 2018, **6**, 14828–14837.
27 J. Xue, Z. Hu, H. Li, Y. Zhang, C. Liu, M. Li, Q. Yang and S. Hu, *Nano Res.*, 2022, **15**, 8819–8825.
28 Y.-K. Li, W.-T. Lu, Y.-X. Du, R. Liu, Y.-T. Yue, Y.-L. Fan, G. Zhang and F.-F. Cao, *Chem. Eng. J.*, 2022, **438**, 135517.
29 Q. Chen and S. Biner, *Acta Mater.*, 2005, **53**, 3215–3223.
30 T. Shen, D. Xiao, Z. Deng, S. Wang, L. An, M. Song, Q. Zhang, T. Zhao, M. Gong and D. Wang, *Angew. Chem., Int. Ed.*, 2024, **63**, e202403260.
31 R. Zerdoumi, A. Ludwig and W. Schuhmann, *Curr. Opin. Electrochem.*, 2024, **48**, 101590.
32 T. Deng, S. Jia, S. Han, J. Zhai, J. Jiao, X. Chen, C. Xue, X. Xing, W. Xia, H. Wu, M. He and B. Han, *Front. Energy*, 2024, **18**, 80–88.
33 H. Shi, Y.-T. Zhou, R.-Q. Yao, W.-B. Wan, Q.-H. Zhang, L. Gu, Z. Wen, X.-Y. Lang and Q. Jiang, *Research*, 2020, 2020.
34 Y. Nie, Z. Li, Y. Wang, X. Zheng, L. Luo, X. Xia, S. Yang, C. Du, Y. Huang and Y. Wang, *Appl. Catal., B*, 2024, **343**, 123494.
35 J. Zhang, M. Yuan, T. Zhao, W. Wang, H. Huang, K. Cui, Z. Liu, S. Li, Z. Li and G. Zhang, *J. Mater. Chem. A*, 2021, **9**, 20676–20684.
36 J. Lan, Z. Wang, C.-w. Kao, Y.-R. Lu, F. Xie and Y. Tan, *Nat. Commun.*, 2024, **15**, 10173.
37 H. Jiang, X. Xie, L. Bi, S. Yu, J. Zeng, L. Zhang, J. Shen and C. Li, *J. Mater. Chem. A*, 2024, **12**, 10385–10391.
38 J. Liu, C. Lee, Y. Hu, Z. Liang, R. Ji, X. Y. D. Soo, Q. Zhu and Q. Yan, *SmartMat*, 2023, **4**, e1210.
39 P. Deka, B. J. Borah, H. Saikia and P. Bharali, *Chem. Rec.*, 2019, **19**, 462–473.
40 H. Chen, M. Nishijima, G. Wang, S. Khene, M. Zhu, X. Deng, X. Zhang, W. Wen, Y. Luo and Q. He, *J. Electrochem. Soc.*, 2017, **164**, F1654.
41 Z. Niu, S. Chen, Y. Yu, T. Lei, A. Dehestani, K. Schierle-Arndt and P. Yang, *Nano Res.*, 2020, **13**, 2564–2569.
42 Z. Xing, J. Li, S. Wang, C. Su and H. Jin, *Nano Res.*, 2022, **15**, 3866–3871.
43 K. Xu, L. Liang, J. Pan, K. Li, B. Zeng, Z. Cui and Q. Liu, *Appl. Surf. Sci.*, 2023, **618**, 156573.
44 C. Wang, D. P. Chen, X. Sang, R. R. Unocic and S. E. Skrabalak, *ACS Nano*, 2016, **10**, 6345–6353.
45 X. Cai, A. Wang, J. Wang, R. Wang, S. Zhong, Y. Zhao, L. Wu, J. Chen and S. Bai, *J. Mater. Chem. A*, 2018, **6**, 17444–17456.
46 P. Zhai, D. A. Cullen and K. Ding, *Chem. Eng. J.*, 2024, **480**, 148238.
47 D. Qu, C. Li, L. Bao, Z. Kong and Y. Duan, *J. Phys. Chem. Solids*, 2020, **138**, 109253.
48 Y. Watanabe, Y. Fujinaga and H. Iwasaki, *Acta Crystallogr., Sect. B:Struct. Sci., Cryst. Eng. Mater.*, 1983, **39**, 306–311.

49 J. Chen, Y.-S. Lai, C.-Y. Ren and D.-J. Huang, *Appl. Phys. Lett.*, 2008, **92**, 081901.
50 C. Wieser, A. Walnsch, W. Hügel and A. Leineweber, *J. Alloys Compd.*, 2019, **794**, 491–500.
51 P. Carlone, A. Astarita, G. S. Palazzo, V. Paradiso and A. Squillace, *Int. J. Adv. Manuf. Technol.*, 2015, **79**, 1109–1116.
52 A. Garg and A. Bhattacharya, *Int. J. Adv. Manuf. Technol.*, 2020, **108**, 1613–1629.
53 W.-B. Wan, T.-Y. Dai, H. Shi, S.-P. Zeng, Z. Wen, W. Zhang, X.-Y. Lang and Q. Jiang, *J. Mater. Chem. A*, 2022, **10**, 4333–4343.
54 D. Bagchi, J. Raj, A. K. Singh, A. Cherevotan, S. Roy, K. S. Manoj, C. P. Vinod and S. C. Peter, *Adv. Mater.*, 2022, **34**, 2109426.
55 W.-L. Hsu, C.-W. Tsai, A.-C. Yeh and J.-W. Yeh, *Nat. Rev. Chem*, 2024, **8**, 471–485.
56 H. Wang, Q.-F. He and Y. Yang, *Rare Met.*, 2022, **41**, 1989–2001.
57 Y. Zhou, R. Zhao, H. Geng, B. Ren, Z. Liu, J. Liu, A. Jiang and B. Zhang, *Coatings*, 2024, **14**, 831.
58 N. Zhou, S. Jiang, T. Huang, M. Qin, T. Hu and J. Luo, *Sci. Bull.*, 2019, **64**, 856–864.
59 E. Trofimov, A. O. Moghaddam, K. Litvinyuk and D. Mikhailov, *J. Alloys Compd.*, 2023, **934**, 168021.
60 D. Wang, Z. Chen, Y. Wu, Y. C. Huang, L. Tao, J. Chen, C. L. Dong, C. V. Singh and S. Wang, *SmartMat*, 2022, **4**, e1117.
61 Y. Wang, N. Gong, H. Liu, W. Ma, K. Hippalgaonkar, Z. Liu and Y. Huang, *Adv. Mater.*, 2023, **35**, 2302067.
62 J. Yu, Y. Yin and W. Huang, *Nat. Synth.*, 2023, **2**, 749–756.
63 J. Wang, J. Zou, X. Hu, S. Ning, X. Wang, X. Kang and S. Chen, *J. Mater. Chem. A*, 2019, **7**, 27514–27521.
64 Y. Wang, J. He, C. Liu, W. H. Chong and H. Chen, *Angew. Chem., Int. Ed.*, 2015, **54**, 2022–2051.
65 Y. Xia, X. Xia and H.-C. Peng, *J. Am. Chem. Soc.*, 2015, **137**, 7947–7966.
66 Y. Yan, J. S. Du, K. D. Gilroy, D. Yang, Y. Xia and H. Zhang, *Adv. Mater.*, 2017, **29**, 1605997.
67 J. Li and S. Sun, *Acc. Chem. Res.*, 2019, **52**, 2015–2025.
68 Y. Yao, Q. Dong, A. Brozena, J. Luo, J. Miao, M. Chi, C. Wang, I. G. Kevrekidis, Z. J. Ren, J. Greeley, G. Wang, A. Anapolsky and L. Hu, *Science*, 2022, **376**, eabn3103.
69 J. S. Blázquez, C. F. Conde and A. Conde, *Int. J. Therm. Sci.*, 2015, **88**, 1–6.
70 M. Zhou, C. Li and J. Fang, *Chem. Rev.*, 2020, **121**, 736–795.
71 K. L. Ngai, J. H. Magill and D. J. Plazek, *J. Chem. Phys.*, 2000, **112**, 1887–1892.
72 W. Chen, R. Yu, L. Li, A. Wang, Q. Peng and Y. Li, *Angew. Chem., Int. Ed.*, 2010, **49**, 2917–2921.
73 S. Han, C. He, Q. Yun, M. Li, W. Chen, W. Cao and Q. Lu, *Coord. Chem. Rev.*, 2021, **445**, 214085.
74 F. Lin, M. Li, L. Zeng, M. Luo and S. Guo, *Chem. Rev.*, 2023, **123**, 12507–12593.
75 C. Peng, J. Ma, G. Luo, S. Yan, J. Zhang, Y. Chen, N. Chen, Z. Wang, W. Wei, T.-K. Sham, Y. Zheng, M. Kuang and G. Zheng, *Angew. Chem., Int. Ed.*, 2024, **63**, e202316907.
76 H. Y. Kim, T. Kwon, Y. Ha, M. Jun, H. Baik, H. Y. Jeong, H. Kim, K. Lee and S. H. Joo, *Nano Lett.*, 2020, **20**, 7413–7421.
77 B. Arumugam, T. Tamaki and T. Yamaguchi, *ACS Appl. Mater. Interfaces*, 2015, **7**, 16311–16321.
78 Y. Yuan, Z. Yang, W. Lai, L. Gao, M. Li, J. Zhang and H. Huang, *Chem. Eur J.*, 2021, **27**, 16564–16580.
79 J. Guo, S. Jiao, X. Ya, H. Zheng, R. Wang, J. Yu, H. Wang, Z. Zhang, W. Liu, C. He and X. Fu, *Chem. Eur J.*, 2022, **28**, e202202221.
80 Q. Gao, H. S. Pillai, Y. Huang, S. Liu, Q. Mu, X. Han, Z. Yan, H. Zhou, Q. He, H. Xin and H. Zhu, *Nat. Commun.*, 2022, **13**, 2338.
81 Q. Gao, B. Yao, H. S. Pillai, W. Zang, X. Han, Y. Liu, S.-W. Yu, Z. Yan, B. Min, S. Zhang, H. Zhou, L. Ma, H. Xin, Q. He and H. Zhu, *Nat. Synth.*, 2023, **2**, 624–634.
82 B. Y. Xia, H. B. Wu, X. Wang and X. W. Lou, *J. Am. Chem. Soc.*, 2012, **134**, 13934–13937.
83 T.-H. Yang, S. Zhou, M. Zhao and Y. Xia, *ChemNanoMat*, 2020, **6**, 576–588.
84 J. K. Mathiesen, E. D. Bøjesen, J. K. Pedersen, E. T. Kjær, M. Juelsholt, S. Cooper, J. Quinson, A. S. Anker, G. Cutts and D. S. Keeble, *Small Methods*, 2022, **6**, 2200420.
85 J. Clarysse, A. Moser, O. Yarema, V. Wood and M. Yarema, *Sci. Adv.*, 2021, **7**, eabg1934.
86 W. Yang, X. Q. Tran, T. Yamamoto, K. Aso, F. Somidin, X. F. Tan, Y. Kawami, K. Nogita and S. Matsumura, *Acta Mater.*, 2022, **224**, 117513.
87 M. Yang, H. Ji, S. Wang, Y.-H. Ko, C.-W. Lee, J. Wu and M. Li, *J. Alloys Compd.*, 2016, **679**, 18–25.
88 H. Y. Jing, H. J. Guo, L. X. Wang, J. Wei, L. Y. Xu and Y. D. Han, *J. Alloys Compd.*, 2017, **702**, 669–678.
89 G. Zeng, S. D. McDonald, Q. Gu, Y. Terada, K. Uesugi, H. Yasuda and K. Nogita, *Acta Mater.*, 2015, **83**, 357–371.
90 J. S. Sun, Z. Wen, L. P. Han, Z. W. Chen, X. Y. Lang and Q. Jiang, *Adv. Funct. Mater.*, 2018, **28**, 1706127.
91 H. Gao, F. Wei, Y. Sui, J. Qi, Y. He and Q. Meng, *J. Mater. Sci.:Mater. Electron.*, 2019, **30**, 2186–2191.
92 X. Zhang, X. Hu, X. Jiang and Y. Li, *Appl. Phys. A*, 2018, **124**, 1–13.
93 X. Peng, Y. Wang, W. Wang, Z. Ye, J. Yang and J. Huang, *J. Alloys Compd.*, 2023, **949**, 169631.
94 Y. Kang, S. M. João, R. Lin, K. Liu, L. Zhu, J. Fu, W.-C. Cheong, S. Lee, K. Frank, B. Nickel, M. Liu, J. Lischner and E. Cortés, *Nat. Commun.*, 2024, **15**, 3923.
95 T.-N. Ye, Y. Lu, J. Li, T. Nakao, H. Yang, T. Tada, M. Kitano and H. Hosono, *J. Am. Chem. Soc.*, 2017, **139**, 17089–17097.
96 M. M. Flores Espinosa, T. Cheng, M. Xu, L. Abatemarco, C. Choi, X. Pan, W. A. Goddard III, Z. Zhao and Y. Huang, *ACS Energy Lett.*, 2020, **5**, 3672–3680.
97 N. Zhang, X. Chen, Y. Lu, L. An, X. Li, D. Xia, Z. Zhang and J. Li, *Small*, 2014, **10**, 2662–2669.
98 Y. Han, Z. Wang, X. Han, W. Fang, Y. Zhou, K. Lei, B. You, H. S. Park and B. Y. Xia, *ACS Sustainable Chem. Eng.*, 2021, **9**, 2609–2615.

99 S. Yan, Z. Chen, Y. Chen, C. Peng, X. Ma, X. Lv, Z. Qiu, Y. Yang, Y. Yang, M. Kuang, X. Xu and G. Zheng, *J. Am. Chem. Soc.*, 2023, **145**, 26374–26382.
100 J. Lim, D. A. Cullen, E. Stavitski, S. W. Lee and M. C. Hatzell, *ACS Energy Lett.*, 2023, **8**, 4746–4752.
101 J. Zhu, L. Hu, P. Zhao, L. Y. S. Lee and K.-Y. Wong, *Chem. Rev.*, 2019, **120**, 851–918.
102 G. Gao, G. Zhao, G. Zhu, B. Sun, Z. Sun, S. Li and Y.-Q. Lan, *Chin. Chem. Lett.*, 2025, **36**, 109557.
103 R. Zhou, Y. Zheng, M. Jaroniec and S.-Z. Qiao, *ACS Catal.*, 2016, **6**, 4720–4728.
104 Z. Deng, Z. Gong, M. Gong and X. Wang, *Nano Lett.*, 2024, **24**, 3994–4001.
105 J. Cheng, C. Lyu, H. Li, J. Wu, Y. Hu, B. Han, K. Wu, M. Hojamberdiev and D. Geng, *Appl. Catal., B*, 2023, **327**, 122470.
106 Y. Ma, M. Sun, H. Xu, Q. Zhang, J. Lv, W. Guo, F. Hao, W. Cui, Y. Wang, J. Yin, H. Wen, P. Lu, G. Wang, J. Zhou, J. Yu, C. Ye, L. Gan, D. Zhang, S. Chu, L. Gu, M. Shao, B. Huang and Z. Fan, *Adv. Mater.*, 2024, **36**, 2402979.
107 X. Li, Y. Chen, X. Zhan, Y. Xu, L. Hao, L. Xu, X. Li, M. Umer, X. Tan, B. Han, A. W. Robertson and Z. Sun, *Innovation Mater.*, 2023, **1**, 100014.
108 D. Raciti and C. Wang, *ACS Energy Lett.*, 2018, **3**, 1545–1556.
109 A. R. Woldu, Z. Huang, P. Zhao, L. Hu and D. Astruc, *Coord. Chem. Rev.*, 2022, **454**, 214340.
110 S. Kuang, M. Li, X. Chen, H. Chi, J. Lin, Z. Hu, S. Hu, S. Zhang and X. Ma, *Chin. Chem. Lett.*, 2023, **34**, 108013.
111 X. Zhang, Y. Zhang, P. Shi, Z. Bi, Z. Shan and L. Ren, *Sci. Total Environ.*, 2021, **770**, 144674.
112 Y. Xiong, Y. Wang, M. Sun, J. Chen, J. Zhou, F. Hao, F. Liu, P. Lu, X. Meng, L. Guo, Y. Liu, S. Xi, Q. Zhang, B. Huang and Z. Fan, *Adv. Mater.*, 2024, **36**, 2407889.
113 X. Zou, J. Xie, C. Wang, G. Jiang, K. Tang and C. Chen, *Chin. Chem. Lett.*, 2023, **34**, 107908.
114 G.-F. Chen, Y. Yuan, H. Jiang, S.-Y. Ren, L.-X. Ding, L. Ma, T. Wu, J. Lu and H. Wang, *Nat. Energy*, 2020, **5**, 605–613.
115 J. Lim, Y. Chen, D. A. Cullen, S. W. Lee, T. P. Senftle and M. C. Hatzell, *ACS Catal.*, 2022, **13**, 87–98.
116 P. H. van Langevelde, I. Katsounaros and M. T. Koper, *Joule*, 2021, **5**, 290–294.
117 S. Zhou, Z. Lv, L. Zhao, D. Zhang, Z. Wang, Y. Dai, B. Li, O. Starostenko, J. Lai and L. Wang, *Nano Res.*, 2024, **17**, 2320–2327.
118 S. Zheng, X. Yang, Z.-Z. Shi, H. Ding, F. Pan and J.-F. Li, *J. Am. Chem. Soc.*, 2024, **146**, 26965–26974.
119 F.-Q. Gong, Y.-P. Liu, Y. Wang, W. E, Z.-Q. Tian and J. Cheng, *Angew. Chem., Int. Ed.*, 2024, **63**, e202405379.
120 Y. He, M. Wang, H. Ji, Q. Cheng, S. Liu, Y. Huan, T. Qian and C. Yan, *Adv. Funct. Mater.*, 2025, **35**, 2413703.
121 Y. Chen, Z. Lai, X. Zhang, Z. Fan, Q. He, C. Tan and H. Zhang, *Nat. Rev. Chem*, 2020, **4**, 243–256.
122 Q. Yun, Y. Ge, Z. Shi, J. Liu, X. Wang, A. Zhang, B. Huang, Y. Yao, Q. Luo, L. Zhai, J. Ge, Y. Peng, C. Gong, M. Zhao, Y. Qin, C. Ma, G. Wang, Q. Wa, X. Zhou, Z. Li, S. Li, W. Zhai, H. Yang, Y. Ren, Y. Wang, L. Li, X. Ruan, Y. Wu, B. Chen, Q. Lu, Z. Lai, Q. He, X. Huang, Y. Chen and H. Zhang, *Chem. Rev.*, 2023, **123**, 13489–13692.
123 B. Chen, Q. Yun, Y. Ge, L. Li and H. Zhang, *Acc. Mater. Res.*, 2023, **4**, 359–372.
124 Y. Ge, B. Huang, L. Li, Q. Yun, Z. Shi, B. Chen and H. Zhang, *ACS Nano*, 2023, **17**, 12935–12954.
125 Z. Li, L. Zhai, Q. Zhang, W. Zhai, P. Li, B. Chen, C. Chen, Y. Yao, Y. Ge, H. Yang, P. Qiao, J. Kang, Z. Shi, A. Zhang, H. Wang, J. Liang, J. Liu, Z. Guan, L. Liao, V. A. Neacsu, C. Ma, Y. Chen, Y. Zhu, C.-S. Lee, L. Ma, Y. Du, L. Gu, J.-F. Li, Z.-Q. Tian, F. Ding and H. Zhang, *Nat. Mater.*, 2024, **23**, 1355–1362.

